ADVANCED TECHNIQUES FOR GAS-PHASE RAMAN SPECTROSCOPY

by

Stephen Biedrzycki

B.S. in Electrical Engineering, University of Pittsburgh, 2009

Submitted to the Graduate Faculty of

the Swanson School of Engineering in partial fulfillment

of the requirements for the degree of

Master of Science in Electrical Engineering

University of Pittsburgh

2011

UNIVERSITY OF PITTSBURGH

SWANSON SCHOOL OF ENGINEERING

This thesis was presented

by

Stephen Biedrzycki

It was defended on

August 16, 2011

and approved by

Hong Koo Kim, Ph.D., Professor, Department of Electrical and Computer Engineering

William Stanchina, Ph.D., Professor, Department of Electrical and Computer Engineering

Steven Woodruff, Ph.D., National Energy Technology Laboratory

Thesis Advisor: Joel Falk, Ph.D., Professor, Department of Electrical and Computer Engineering

ADVANCED TECHNIQUES FOR GAS-PHASE RAMAN SPECTROSCOPY

Stephen Biedrzycki, M.S.

University of Pittsburgh, 2011

The small cross-sections associated with Raman scattering generally hinders the application of Raman spectroscopy to low density gas analysis. The focus of this work is the development of tools and techniques to enhance collection of Raman-scattered light from gaseous samples contained in hollow-core waveguides. The developments are motivated by a need for accurate, real-time composition analysis of natural gas for clean and efficient turbine operation. Methods to increase the Raman signal and to reduce system noise sources are explored. Silver-coated silica waveguides currently used are covered with a highly fluorescent protective plastic coating which is responsible for most of the system noise. One noise reduction method explored is the replacement of these guides by polished, pure or sterling silver tubes. Work directed toward increasing Raman signals began with an analysis of the modal properties of the hollow waveguides used to contain the Raman medium. This work enabled the optimization of Raman power output and the design of the system's collection optics. Other efforts include development of a new statistical algorithm that applies principal component analysis to extract the gas composition from a collected Raman spectrum. A novel apparatus replaced the spectrometer normally employed in a Raman sensor system by tunable optical filters in a derivative of wavelength modulation spectroscopy.

TABLE OF CONTENTS

LIST OF TABLES

LIST OF FIGURES

PREFACE

I would like to acknowledge the mentorship by Michael Buric whose guidance provided a head start on my research and helped me avoid many pitfalls I would have otherwise struggled with in the lab.

1.0 INTRODUCTION

The globalization of the fuel economy has introduced the need for flexibility in turbine operation. The operation of natural gas turbines in particular is sensitive to fuel mixture changes. Stable and efficient operation of such turbines becomes increasingly difficult when energy content of fuels changes as different global sources mix in the pipelines. A growing trend is the introduction of alternative fuels and fuel mixes in general-use turbines. An example is Syngas, a mixture whose active components are carbon monoxide and hydrogen. Syngas is synthesized from natural gas, biomass, or through coal gasification and is becoming more common as a fuel source. The densities and energy content that result from various fuels mixing leads to fluctuations in flame speed which, if not accounted for in the fuel and air intakes, results in uneven burn or incomplete combustion.

Operators desire accurate fuel content information updated every second in order to adjust fuel valves to maintain uniform flame speeds. The values of concentrations of fuel gases as well as select minorities such as nitrogen, oxygen, and carbon monoxide are desired within one percent accuracy for characterization of flame speed. The current technology was not designed to meet these strict control requirements so operators look to new technologies that offer speed and accuracy beyond what is currently available. Although gas chromatography and mass spectroscopy are capable of measuring all gases of interest, even the fastest systems are too slow to use for system control [1][2]. Raman sensing is applicable to fuel gas analysis, however

the small signals available pose a hurdle to developing a sensor system that meets the required specifications. The work presented here investigates techniques to enhance a Raman spectroscopy-based gas sensing system that aims to fulfill the requirements necessary for turbine control.

Raman spectroscopy applies the identifying properties associated with Raman scattering. Raman scattering from molecules provides the means to probe the vibrational frequencies of a sample using an excitation light source. A detailed explanation of Raman scattering can be found in [3], however a brief explanation follows. A molecule experiences an induced dipole moment $\mu_{induced}$ in an external electric field

$$\mu_{induced}(t) = \alpha E_0 \cos(2\pi\nu t)$$

where ν is the excitation frequency, E_0 is the electric field magnitude, and α is the polarizability of the molecule. The polarizability is a function of bond length and can be expressed after a Taylor expansion as

$$\alpha(x) = \alpha(x_0) + x(t)\left(\frac{d\alpha}{dx}\right)_{x=x_0} + \cdots$$

where the bond length *x(t)* is a function of the molecule's vibration, at frequency ν_{vib} , around its equilibrium position x_0 and is described as

$$x(t) = x_{max}\cos(2\pi\nu_{vib}t).$$

Combining the two previous expressions and simplifying provides the complete expression for the induced dipole moment

$$\mu_{induced}(t) = \alpha(x_0)E_0\cos(2\pi\nu t) + \left(\frac{d\alpha}{dx}\right)_{x=x_0} x_{max}\frac{E_0}{2}\left[\cos\left((2\pi\nu + 2\pi\nu_{vib})t\right) + \cos((2\pi\nu - 2\pi\nu_{vib})t)\right]$$

The reemitted light takes on the same frequencies as the dipole moment giving Rayleigh scattering at ν, Stokes scattering at $\nu-\nu_{vib}$, and anti-Stokes scattering at $\nu+\nu_{vib}$. The collection of the Stokes or anti-Stokes scattered light provides information about the vibrational modes of the sample gas which are essentially unique for small set of molecules of interest enabling gas identification.

From the previous analysis, the condition required for Raman scattering is $d\alpha/dx \neq 0$ which turns out to be true for many vibrational modes. This condition is quite flexible in comparison to the requirement for IR absorption spectroscopy, $d\mu/dx \neq 0$, which prevents the application of IR spectroscopy to the detection and measurement of symmetric diatomic gases. The detection and measurement of N_2, O_2, and H_2 are particularly important in fuel gas analysis as studied in this work although this advantage extends to all symmetric diatomic gases. The ability to detect and measure diatomic gases opens possible uses in industrial chemical processing. There are other chemical sensing applications which make this Raman-based system desirable as the system's flexibility enables a wide range of detection possibilities. These alternative applications include Syngas production, toxic chemical processes, ammonia manufacturing, sulfur processing, and numerous others.

A diagram showing the energy levels associated with Raman scattering and IR absorption spectroscopy is provided in Figure 1. The probability of scattering is proportional to the number of occupied states which is described by the Boltzmann distribution. For the most accurate measurements it is thus better to collect and measure the Stokes Raman as the intensity will be stronger than anti-Stokes emission. Additionally, the relation of the Stokes to anti-Stokes Raman emission can be used to calculate the sample temperature using the Boltzmann relation adding further flexibility to the sensor's applications. Generally, the temperatures common to Raman

sensing will not significantly populate the higher energy levels to produce strong anti-Stokes Raman emission. For this reason, Raman sensing utilizes the Stokes scattering almost exclusively.

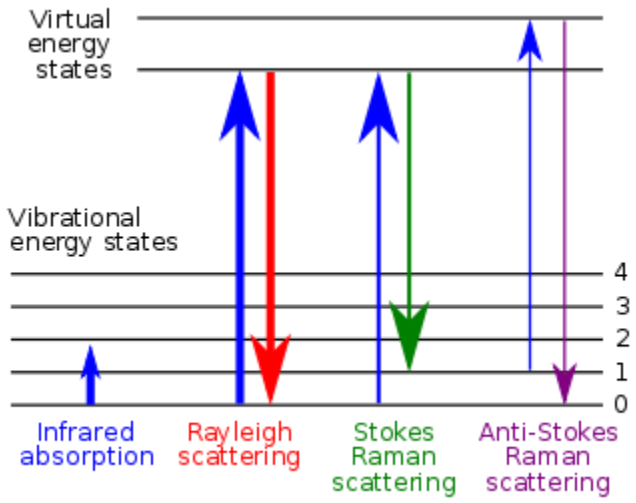

Figure 1 - Energy level diagram of Raman and IR spectroscopy [4]

A Raman spectrometer collects scattered light from a sample illuminated by a laser light source. The high particle density of liquids and solids provides significant Raman signal with moderate laser powers. A common configuration for performing gas phase Raman analysis is shown in Figure 2a. The lower density of gas limits efficient scattering of the laser light as Raman resulting in it being difficult to detect signals. At such low levels, long integration times and high laser power is necessary to capture enough light to perform accurate characterization of the sample. The introduction of a hollow waveguide for containing the sample gas and collecting scattered Raman emission enabled fast and accurate gas sensing [5]. One such sensor configuration using the hollow waveguide is shown in Figure 2b.

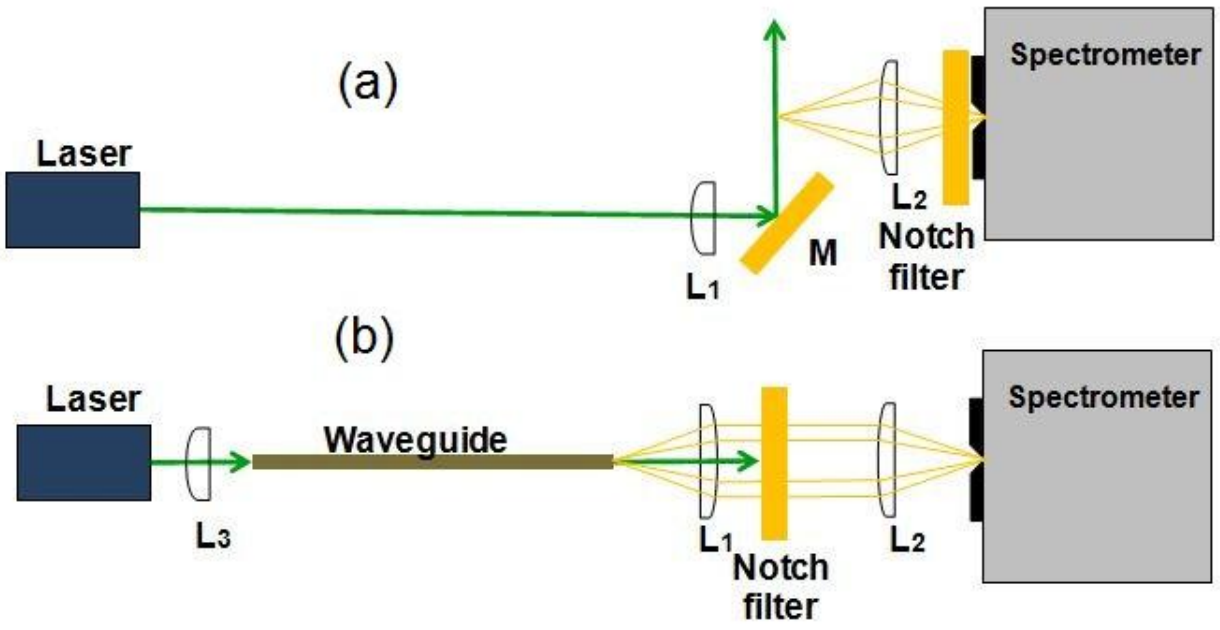

Figure 2 - Gas phase Raman sensor configurations (a) Free space and (b) Hollow waveguide

The introduction of the hollow waveguide is just one technique used to increase the total collected Raman signal. The hollow waveguide increases the interaction length of the pump light to increase the scattering efficiency of the system. Proper selection of the system optics enables increased collection angles that also enhance the system efficiency. In contrast to solid or liquid phase Raman spectroscopy, these principles are necessary to achieve high accuracy with a limited integration time as very little pump light is Raman scattered by the sample.

A number of techniques and enhancements have been investigated for improving the functionality of the gas phase Raman sensor. Section 2 provides additional information on the use of hollow waveguides in this sensor system. Section 3 addresses the influence of system noise on the small measured Raman signals and what approaches were taken to minimize noise sources. Alternative waveguide fabrication processes to reduce system costs were explored in Section 4. The modal characteristics of hollow metal-lined capillary waveguides are theoretically examined and experimentally confirmed to provide design parameters for optimizing system

performance. This waveguide analysis is covered in Section 5. In an attempt at further reductions in system cost, a replacement for the spectrometer was considered. A tunable band pass filter was used for isolating the Raman line. Tuning was accomplished by rotating the filter. The design and analysis of the rotating filter spectrometer system is covered in Section 6. Finally, a method of quantifying gas composition statistically from observed spectra was developed using principal component analysis. This method and derivation are covered in Section 7.

2.0 OVERVIEW OF GAS-PHASE RAMAN TECHNIQUES

Gas phase Raman spectroscopy offers a great challenge compared to Raman spectroscopy in liquids and solids. The generally low probability of Raman scattering is further exacerbated by the low particle densities in gaseous samples. With efficiencies as low as 10^{-13} [6], collecting measurable Raman power is exceptionally difficult using a free space Raman configuration. Obtaining the necessary Raman power to quantify gas concentrations at speed desired for burner control requires a number of additional techniques to maximize collection efficiency.

The primary functional change from a free space Raman configuration in the sensor system is the unique analyte cell. A hollow waveguide contains the flowing gas sample while guiding the pump laser light and collecting the scattered Raman light. The combination of light guiding and analyte containment enables very long interaction lengths to increase the collectable Raman power by nearly 3 orders of magnitude [5]. The earliest investigation of this configuration used hollow core photonic bandgap fibers. One advantage of such fibers is that the losses are so low that the fibers enhance Raman collection linearly with the length of the fiber. The growing popularity of bandgap fibers offered a solution for a low cost sensing cell.

More recent work has moved in the direction of hollow metal-lined waveguides. Obtaining accurate gas concentration in a short time requires both high collection efficiency and fast sample rates. The large diameters of metal-lined waveguides have the distinct advantage of supporting high gas transfer rates necessary for update times as fast as one second. A diagram of

such a waveguide is shown in Figure 3. They have a typical radius between 150 and 350 microns, lengths as long as 2 meters, and are often have aluminum or silver metal linings. Characterizing the Raman collection of these waveguides is necessary for system optimization. For this reason, theoretical analysis of the waveguide modes was studied to accurately predict the collected Raman power for given waveguide dimensions and metallization. A series of experiments was performed to verify the accuracy of the theoretical analysis and is covered in detail in Section 5.

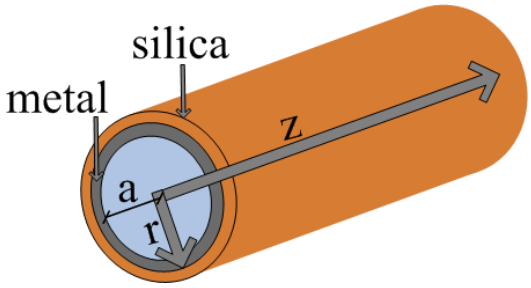

Figure 3 - Diagram of a hollow metal-lined capillary waveguide

On the measuring end of the Raman sensing system sits a Horiba JY iHR550 spectrometer with a CCD array. Optimization of the spectrometer configuration is performed through careful analysis of the collection of light at the input slit. The light collected from the hollow waveguide forms a circular image whose angular spectrum must fit within the angular acceptance of the spectrometer. The magnification of the image enables reducing the angular distribution of the collected Raman. The drawback of magnification is the loss of resolution and possible collection efficiency. With increased magnification less light fits in the slit so the magnification must be balanced for a particular resolution desired. This trade off leads to challenges since additional consideration is required when selecting a waveguide diameter as its size will factor into these calculations.

An alternative technique provides the means to fit the angular spectrum to the spectrometer with no resolution loss. The use of a fiber optic bundle with a round aperture on one end and a rectangular aperture on the other, as shown pictorially in Figure 4, fits the capillary image to the profile of the spectrometer slit. The magnification is then selected to completely fill the fiber bundle input end to minimize the angular spread at the spectrometer while retaining a slit width equal to the width of the fiber, 250 microns. The fiber bundle provides flexibility when selecting capillary diameters as larger magnifications are possible without loss of light collection at the spectrometer slit.

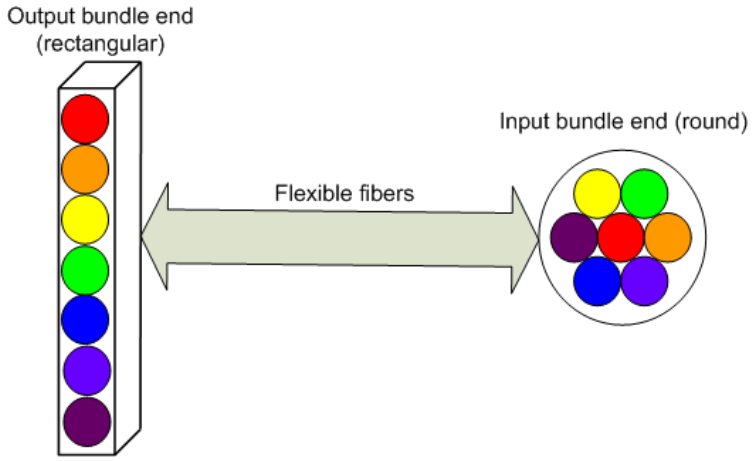

Figure 4 - Schematic of the fiber bundle

Upon reaching the CCD array, a Princeton Instruments 2-dimensional array with 25 micron pixels arranged in 252 rows and 1024 columns, the spectrum is recorded as a 1-dimensional vector by summing the CCD array columns. This provides a simple spectrum from which the gas concentrations are determined by measuring the intensities of the peaks. The advantage of performing the column summation is that this technique uses the minimum silicon area for measuring the rectangular input image. This minimizes the dark noise associated with individual points for maximum signal to noise ratio. The minimization of noise is especially important due to the small signals associated with Raman scattering.

Minimizing detector noise is just one of the ways that the system is optimized to meet the desired detection limits and collection times. Reducing or eliminating noise sources is utilized to the greatest extent possible to obtain a very high signal to noise ratio. Although increasing the pump power can reduce the significance of noise, greatly reducing or eliminating the noise sources provides a significant reduction in detection limits and collection times as well as flexibility in system design. Short pump wavelengths seem desirable as Raman efficiency is inversely proportional to λ^4 but the increased fluorescence associated with short wavelength pumping limits the value of this technique. Elimination of fluorescence would open up the possibility of a large increase in system efficiency by using a 466 nm diode laser. Methods of characterizing and reducing system noise are explored in more detail in the next section.

3.0 NOISE ANALYSIS AND REDUCTION

As a part of implementing general system improvements, early methods of increasing the signal to noise ratio focused on reducing the large noise levels encountered with the typical system configuration. The sources of noise were identified and characterized in an effort to reduce or eliminate their contribution to measured spectra. We sought to minimize the two optically excited noise sources, silica Raman and fluorescence. The silica walls of the capillary capture a portion of the pump and emit Raman scattered light that is collected by optics. As with the silica walls, the polyimide coating over the silica fluoresces when excited by the pump. The other two sources, dark and readout noise, were characterized in order to account for their contribution and subtract them out from recorded spectra.

The first sources investigated were also the largest: the wideband fluorescence and silica Raman. Initially, the fluorescence and the silica Raman were believed to contribute to the wideband noise and the aim was to limit how much could be excited and what portion of it would be collected. Identifying where the light is generated was the first effort in minimizing how much is captured. In this effort, a silver colloidal paint from Ted Pella was selected to provide a reflective coating that would limit the amount of light that could enter or exit the silica glass structure of the waveguide at the capillary end face. The theory was that fluorescence and silica Raman generated along the waveguide could be guiding in this layer and captured by the collection optics. Experiments were performed to analyze the effect of the colloidal paint.

Figure 5 shows the results of using paint on two different capillaries. The noise levels are reduced to about a quarter of the bare capillary faces with no significant difference between the two capillary lengths tested. This indicates most of the noise is coming from near the capillary face emphasizing the need to suppress this noise source for short capillaries to achieve high signal to noise. Colloidal graphite paint was also attempted but was quickly abandoned for a few reasons. The graphite is no more effective than the silver paint but it is more difficult to apply evenly. It also has the inherent problem that if it enters the end of the capillary it would increase losses due to its high absorption.

Another investigation of noise sources was conducted after noticing unexpected noise present in a test using a sterling silver capillary as a waveguide replacement for the Doko capillaries. Noise levels were measured after removing the capillary from the system and comparing noise levels at varying integration times. The presence of what appeared to be fluorescence noise led to the discovery that the ferrules that secure the capillaries in the nano-positioning stage introduced significant noise above dark levels. The ferrules form an airtight seal around the end of the capillary. Their proximity to the waveguide entrance aperture allows a portion of the pump to illuminate them and excite fluorescence. A comparison of the three available ferrules was performed to find the best choice for minimal noise.

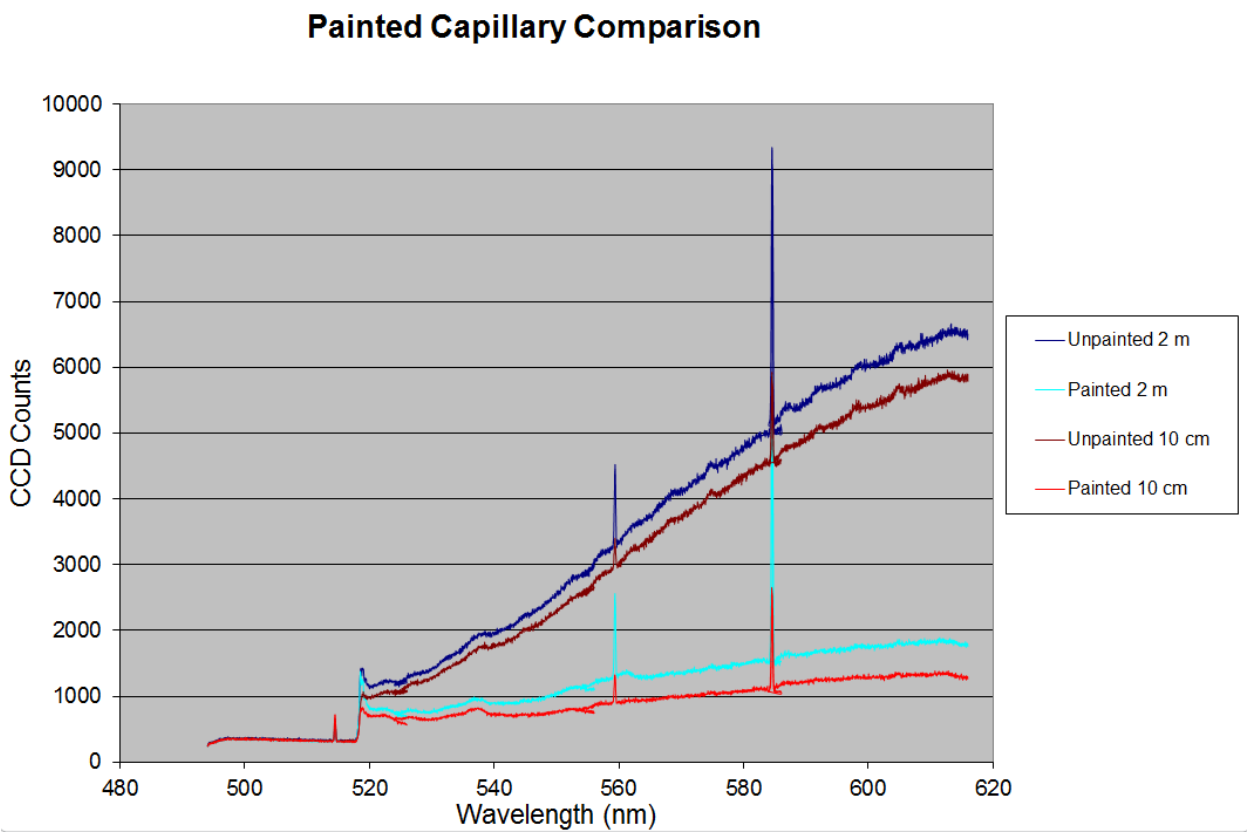

Figure 5 - Painted capillary end noise reduction

Figure 6 shows a graph of the three ferrules tested with the dark noise level shown for comparison. Both the pure graphite and pure vespul ferrules show significant noise while the mixed graphite/vespul ferrules are almost indistinguishable from dark levels. A binder that is used in the production of the pure graphite ferrules could account for the suspected fluorescence noise. The mixed material ferrule is the preferred choice for minimizing noise; however, the ferrule face is painted using the colloidal silver paint as done with the capillary face to eliminate fluorescence entirely.

Painting the capillary face and the ferrule reduces the noise to far lower levels than without; however, there the presence of wideband noise indicates the solution is imperfect. In order to reduce the noise to that of dark and readout noise a closer examination of the capillary

materials was conducted to determine if an alternative is preferable. The first task isolated the source of the noise by examining the protective polyimide coating.

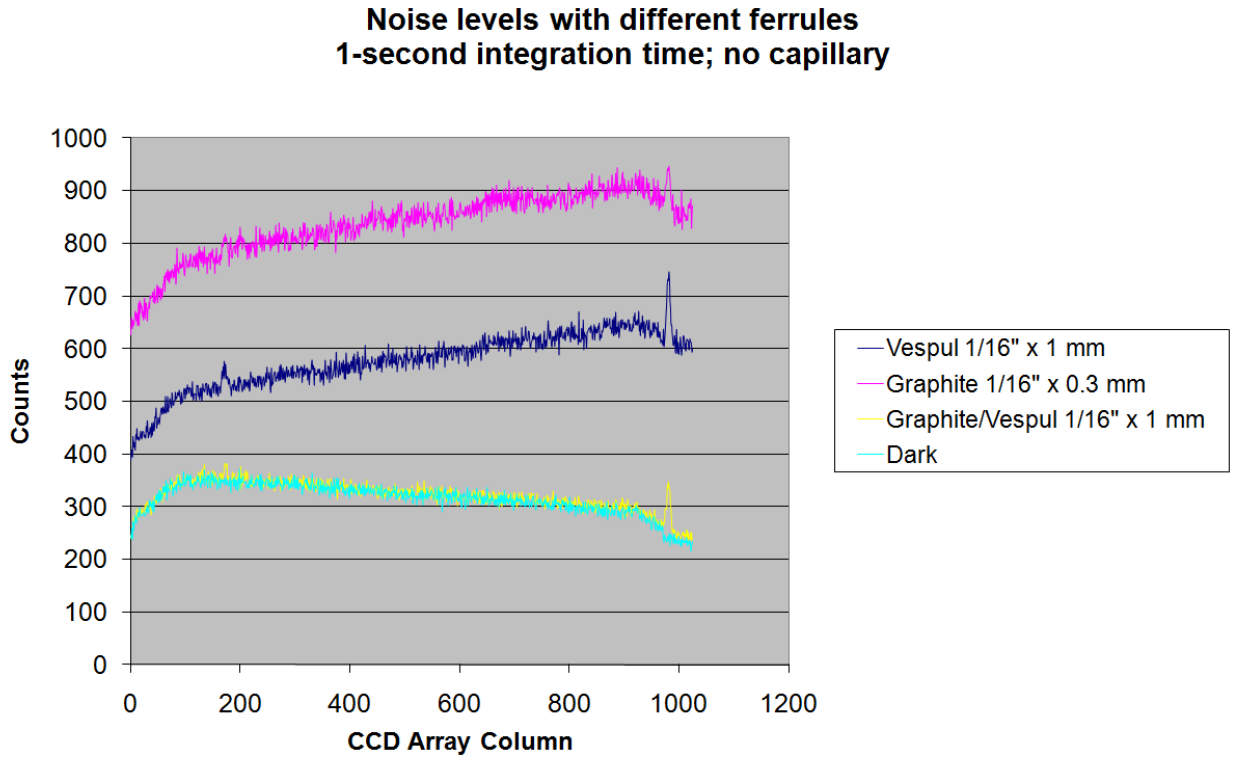

Figure 6 - Ferrule noise

An experiment was setup to focus laser light on either the polyimide coating or the inside silver layer only. This was done by stripping back the coating of the end of a capillary and inserting the piece perpendicular to the beam path. This enabled the measurement of the noise levels when the laser is incident only upon the silver and the polymer layer that protects it from oxidation. The resultant spectra were indistinguishable from dark levels. Repeating the experiment with a piece of the capillary with the coating and silver removed also showed no wide-band noise in the range of the relevant Raman peaks. Performing the experiment using a piece of the polyimide coating only, however revealed the wide-band noise seen in typical Raman spectra using the system. From this we learn that silica Raman does not contribute

significant noise in the range of the gaseous Raman peaks that are of interest and the noise we want to suppress is generated almost entirely by the protective polyimide capillary coating.

Confirmation of the polyimide coating as the source of noise led to interest in either removing the coating or finding an alternative capillary system that would not emit fluorescence when excited by the pump wavelength. Coating removal was examined using open flame and a temperature controlled oven. Although the coating is easily burned away using an open flame, complete removal is impossible without doing harm to the reflective silver layer. A number of attempts were made using a temperature controlled oven to carbonize the material and brush it away. Temperatures around 600 °C were sufficient to remove the coating, but surprisingly, they were also sufficient to remove the silver layer. The thin layer of silver was not expected to melt as bulk silver has a melting point of nearly 1,000 °C.

One final method was tested to remove the coating. KrF excimer laser ablation of the polymer effectively removed the coating without causing apparent damage to the silver layer. For bulk processing, a significant amount of time would be required to carefully remove the coating along the entire capillary. Such processing was not attempted due to the drawbacks of removing the coating which became apparent throughout the experimentation with coating removal. The polyimide coating provides flexibility to the waveguide. Removal of the coating leaves the waveguide extremely fragile such that a few trials at coating removal were ruined by cracked capillaries. Although careful handling could enable the waveguides to function well in the system, the extreme sensitivity to shock limits the waveguides value in the system. For these reasons we chose to explore alternative coating options that would eliminate the fluorescence without sacrificing the waveguide durability.

A comparison of alternative capillaries was performed to examine the noise and evaluate the possible substitutes. The first tested was a polished sterling silver jeweler's tube, 30 cm long with a 500 μm internal diameter. With no glass or plastic jacket, these capillaries were not expected to emit any optically excited noise. The jeweler's capillary was compared to a 30 cm long Doko capillary of 530 μm internal diameter. Even though the Doko capillary showed nearly 20 times the power transmission, it only had about twice the Raman signal-to-noise of the silver tube due to the large difference in fluorescence. If the transmission can be improved to match that of the Doko capillary such a waveguide would prove to be an excellent replacement. Production of waveguides using silver capillary tubing is examined in detail in Section 4. The vespul/graphite ferrule was used in these experiments to limit it as a source of noise. Figure 7 shows measured spectra for the two waveguides showing the difference in fluorescence noise.

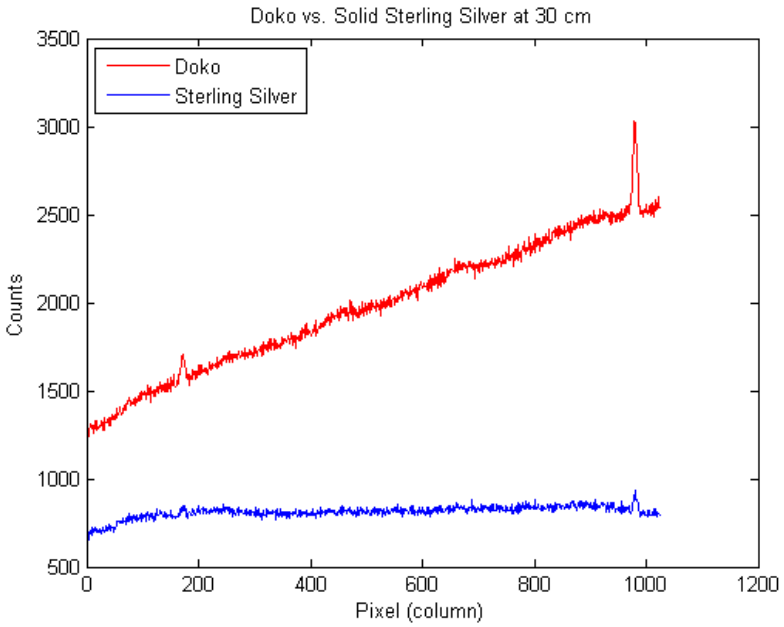

Figure 7 - Noise level comparison between the Doko and Silver Jeweler's Tube

Two capillaries produced by Polymicro were also examined as potential substitutes [7]. The first had a AgI/Ag internal coating at 300 um internal diameter (HWEA300750). The

approximately one meter long piece had just over 11% transmission. The input 514.5 nm power had to be reduced to 30 mW input since the tube face burnt and the glass cracked when the full 65 mW power available was incident on the tube entry. The acrylic coating produced significantly more fluorescence noise than the Doko capillary with noise greater than 300,000 counts per second. Similarly high fluorescence noise was found in the other Polymicro capillary which had a 50 μm internal diameter (LTSP050375). This capillary features a polyimide coating over a doped silica/silica tube. The noise totaled more than 400,000 counts per second. This capillary did not have a silver coating which may have allowed light to leak into the polyimide layer.

Two other Polymicro capillaries were examined that offered UV transparent coatings. Such capillaries are marketed for their minimal fluorescence at short wavelengths. These coatings matched their specifications and showed no signs of fluorescence in our tests. They would serve well as replacements for the polyimide coated capillaries if silver-lined variants are available. As of the date of writing, no such variant is available so custom silver deposition techniques must be developed to create suitable waveguides using these coated capillaries.

The final step in noise analysis involved characterizing the noise associated with our CCD array. This was done for the sake of completion as well as providing baseline spectra that can be used to subtract the noise background introduced by the detector. There are two noise sources introduced by a CCD array, readout and dark noise. Readout noise is a small statistical error associated with reading data from the array's amplifier. Dark noise, or dark current, is the introduction of additional electrons to the measured signal due to thermal emission. The measured dark noise is a linear function of time as longer integration times allow for additional thermal electrons to accumulate.

The readout noise was measured first out of simplicity. Ten measurements were taken each with 10 ms integration time. The readout noise for each column/pixel is taken as the mean of the 10 measured values with the assumption that the dark noise is insignificant at such a short integration time. The data was collected under the two different CCD configured modes; Figure 8 shows the readout noise using column summation and Figure 9 shows the readout noise associated with individual pixel readout. The experiments were done using both modes to verify our intuition of the automatic column summation's effect on total noise.

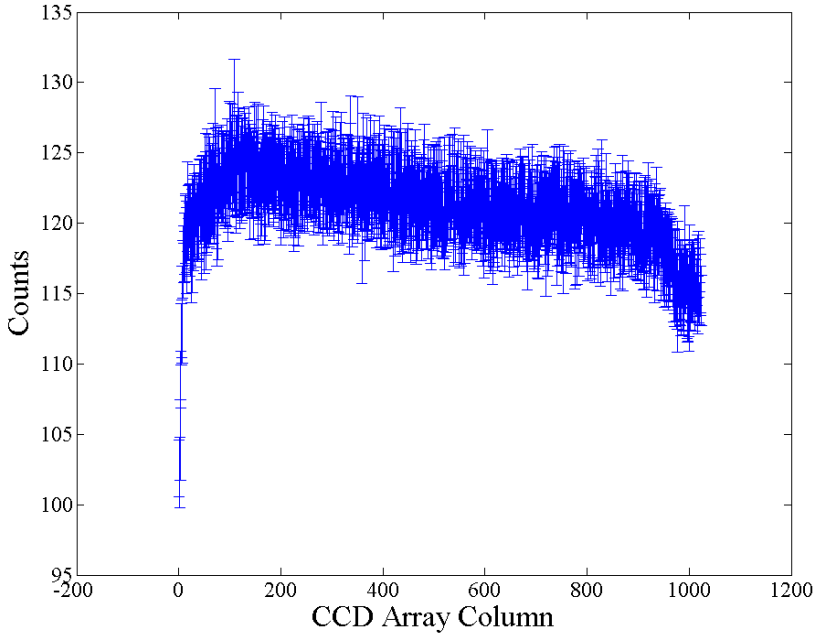

Figure 8 - CCD readout noise with column summation

Note the measurement was taken in the dark and little to no light is measured during the short measurement time and we expect little dark noise at such a short integration time. The error bars shown in the figure are + and – rms values of the 10 measured values calculated as the standard deviation of the collected data. If we assume that the readout noise is Poisson distributed the rms values should be the square root of mean number of counts. Experimentally this is correct as one can discern from the graphs. The streaking phenomena, the principle that

measurements at the lower pixels accumulate counts while waiting to readout, appears in Figure 9 as an increase in the average readout noise from 98 counts near the top of the array to 102 counts near the bottom. This may result from dark noise that occurs during the readout time of the array as the entire readout can take nearly a second.

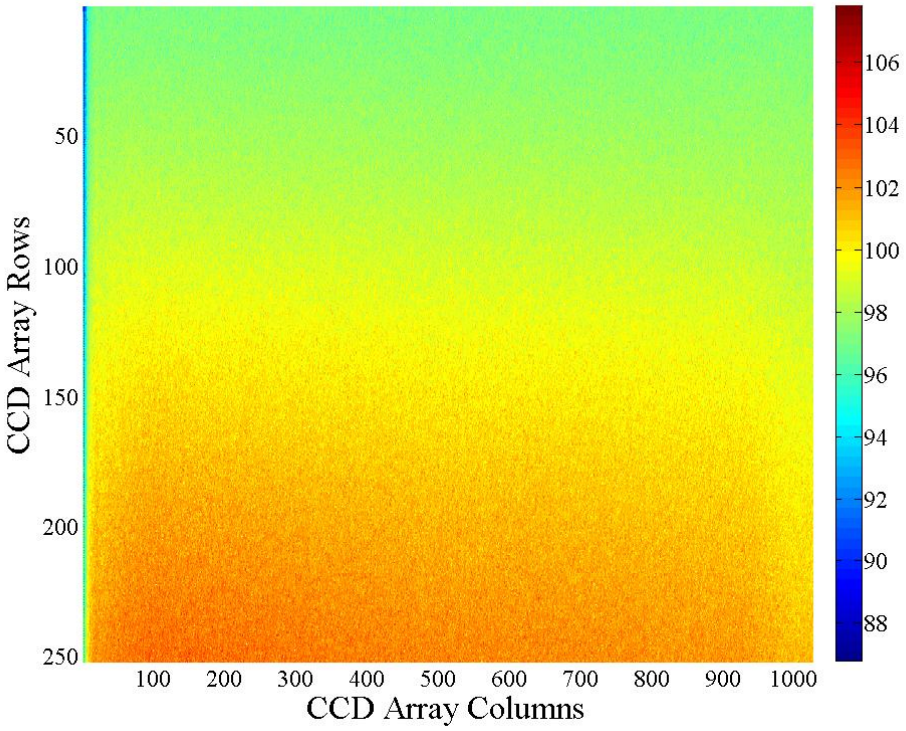

Figure 9 - CCD array pixel readout noise

Finding the dark noise at each column/pixel is done by calculating the slope of the noise across multiple integration time measurements. Ten measurements were taken at each integration time: 1, 5, 10, 25, 45, 60, and 120 seconds. The 7 time measurements were collected to produce 10 line graphs representing the noise as a function of time. A linear fit was calculated for each case and the slope was recorded. The dark noise is found by finding the mean of the 10 slopes and a standard deviation is also calculated. The data for column summation and the complete array are shown in Figure 10 and Figure 11, respectively. Given that dark noise

increases with temperature, we can see from the two plots that the detector temperature is not perfectly uniform across the entire array. This information can be used to position the spectrometer grating to minimize the dark noise in noise sensitive experiments.

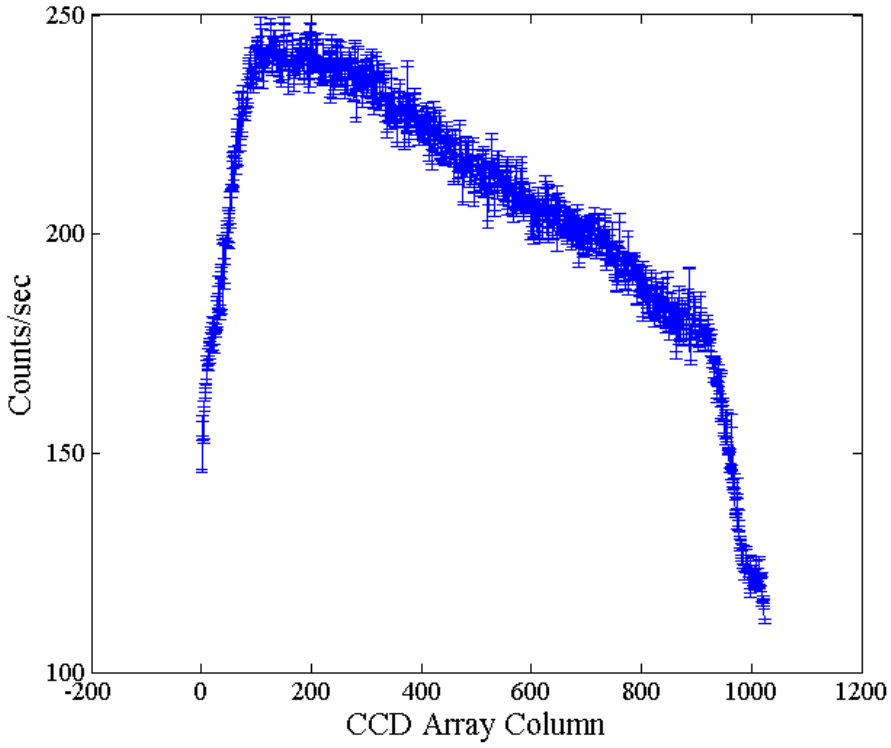

Figure 10 - CCD dark noise with column summation

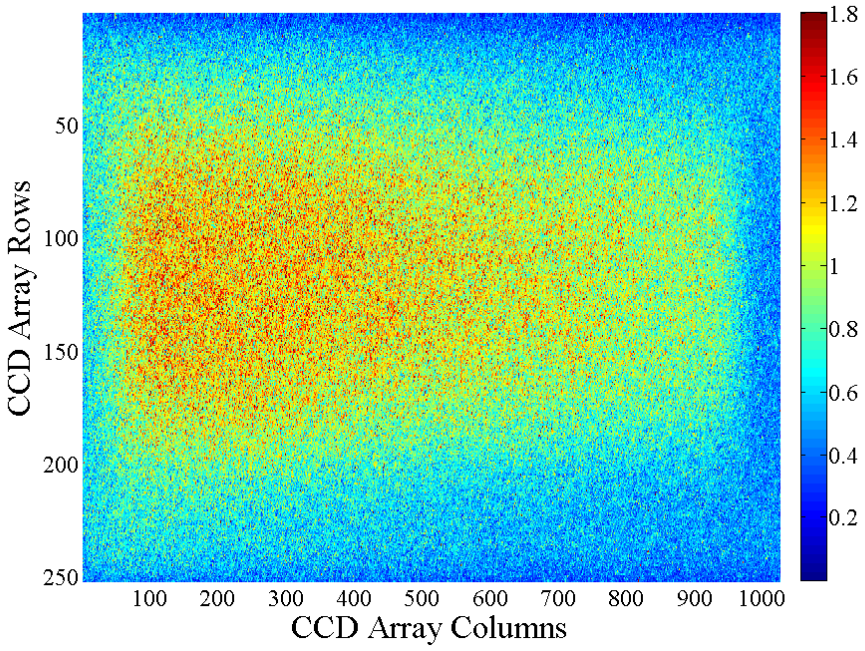

Figure 11 - CCD array dark noise per pixel

Our expectations for the noise response in each case are confirmed by these results. The readout noise is approximately the same whether reading an entire column or individual pixels; however, the dark noise adds as expected. This result demonstrates that it is preferable to have the array perform column summation internally instead of external processing as this would multiply the effect of the readout noise.

As this analysis shows, the noise response of the detector can vary across the entire collection area. This variation leads to areas of greater signal to noise ratio due to reduced noise levels. Applications that do not require the entire array can take advantage of this information to maximize the signal to noise ratio for the wavelength of interest. Coupling the low detector noise with the noise suppression provided by the colloidal paints reduces the detection limit of the sensor for a given collection time. Each incremental gain in noise suppression contributes significantly to the maximizing the signal to noise ratio. For this reason, alternatives were considered to the Doko capillary to eliminate it as a noise source entirely.

4.0 SILVER CAPILLARIES AS AN ALTERNATE WAVEGUIDE

The high fluorescence noise associated with the polyimide coating significantly reduces the signal to noise ratio for most Raman measurements using the Doko waveguides. The costs and challenges of removing the coating spurred an interest in replacing the capillaries with an alternative waveguide. Silver is the preferred waveguide material due to its low losses over the visible and near-IR spectrum so it was natural to consider all silver waveguides. The use of silver capillaries eliminates both fluorescence noise as well as the silica Raman associated with the glass capillary wall.

In addition to the lack of noise, silver capillary waveguides are cheaper if fabricated with our techniques described in this section. Our starting point was the examination of low cost sterling silver capillary tubing purchased from OttoFrei, a jewelry supplier. At only a few dollars per foot of capillary, these would be far cheaper waveguides if a simple polishing process is sufficient to make them suitable for visible light guiding. Three polishing options were explored, one chemical polishing process and two mechanical polishing compounds. Although the chemical technique is the most involved process, it originated for IR waveguide fabrication in 1992 [8].

The chemical polishing method takes advantage of the smoothing effect of chemical reactions on rough surfaces. The reaction with the rough sterling silver walls removes sharp peaks and deep valleys. The complete process is done as a number of steps involving flowing

different polishing and cleaning solutions through the capillary. The capillary is initially cleaned by flowing through a solution of methanol followed by a solution of ammonium hydroxide to remove any natural oxidation layer. The polishing process consists of three primary chemical solutions. An etchant solution, composed of 80 mL sulfuric acid and 20 mL nitric acid diluted ten times, is used to etch away the exposed copper on the sterling tubing inner surface. Following etching, a polishing solution of 55 grams of chromium oxide, 1 ml of hydrochloric acid, and 200 mL of deionized water diluted 10 times is pumped through the capillary in cycles. The polishing solution forms a layer of silver chloride which is removed by subsequent cleaning procedures using ammonium hydroxide. The polishing step is repeated as needed to produce a reflective surface.

After polishing the inner capillary wall a layer of silver iodide is often formed both to protect the silver from oxidation and to form a highly reflective layer that reduces propagation losses. This process requires careful control of the solutions flowing through the capillary. Iodine flowing through the silver capillary reacts with the silver walls to produce a growing layer of silver iodide. Careful control of the layer thickness provides a highly reflective surface for the desired wavelength. However the timing of this process is difficult for visible wavelength guiding so this was only attempted once comfortable with the polishing process. One example of a capillary polishing procedure is shown in Table 1. Depending on the characterization results and observed Raman-detection-system noise levels, additional ultrasonic cleaning in ammonium hydroxide was performed when needed.

Table 1 - Example polishing procedure

Step	Chemical	Processing method	Time
1.	Deionized water	Pumped	10 minutes
2.	Methanol	Pumped	10 minutes
3.	Ammonium hydroxide	Ultrasonic bath	30 minutes
4.	Deionized water	Ultrasonic bath	20 minutes
5.	Etchant solution	Pumped	15 minutes
6.	Deionized water	Pumped	5 minutes
7.	Polish solution	Pumped	10 minutes
8.	Deionized water	Pumped	5 minutes
9.	Ammonium hydroxide	Pumped	20 minutes
10.	Deionized water	Pumped	15 minutes
11. Repeat steps 5 through 10 after testing and characterization as needed			
12.	Methanol	Pumped	15 minutes
13.	Iodine solution	Pumped	15 seconds
14.	Methanol	Pumped	15 minutes

The complete polishing procedure was performed on three separate sterling silver capillaries to test the effects of different solution concentrations and polishing and etch timings. The original polish solution was later diluted further to slow the reaction down to reduce clogging and provide more control over the reaction rate. The original polish time was selected according to the suggested time in [8]. The cycles were repeated with periodic 514.5 nm light transmission testing to gauge progress. Although slight improvements were detected, pump transmission was never comparable to the Doko capillaries. A typical Doko capillary of equivalent length has between 80 and 90 percent pump transmission while the best case transmission from a chemically polished sterling capillary was only 30 percent. Without achieving low enough losses for pump propagation there was no hope for reducing the losses of the high order Raman modes necessary for efficient collection. The chemical polishing method,

although suitable for making IR waveguides, is not sufficient for producing optical waveguides and so it was abandoned.

Mechanical polishing methods were explored due to the relative simplicity of the process compared to chemical polishing. A suspension of abrasive compound pumped through the capillary removes the sharp edges to produce a specular surface. Two compounds were selected from Ocean State Abrasives to test the effectiveness for making Raman waveguides. A liquid suspension which has a very fine abrasive specifically designed for high quality mirror coatings was selected to obtain the best surface quality to minimize losses for the high order modes. A 2 micron cerium oxide abrasive was also selected as the particle size would be sufficient to provide a fair surface quality while requiring a reasonable time to complete the polishing process in the event that the liquid polish is too slow.

The first polishing attempt began with a dilution of the liquid polish to ensure the pump would not become clogged throughout the polishing process. After developing some confidence in the setup, the system was run using undiluted liquid polish while operating overnight to speed up the process. Initial tests showed significant improvement in the pump laser power transmission. Using the capillary for Raman collection was not very successful in some of the early tests as it was discovered that significant cleaning was needed after each polishing cycle otherwise Raman- system noise levels would interfere. About 60% pump transmission was achieved after 30 hours of polishing and reached as high as 65% after 50 hours. The capillary was polished for a total of 100 hours but no significant improvements were found after 50 hours of polishing. The primary limitation encountered with the mechanically polished capillaries was the limited Raman enhancement. Even though pump transmission increased significantly, the

collected Raman power increased by only 20% which leaves the total power collected at less than a tenth of what is possible in a comparable sized Doko capillary.

Finding no gains using the liquid polish beyond 50 hours led to speculation that the process is too slow using the fine polishing solution. A second test was started using a 5% suspension of 2 micron cerium oxide. The test would explore the possibility that a larger grain abrasive would polish faster and obtain a high quality specular surface where the theory was that the liquid polish may require a few hundred hours to produce the desired surface roughness. The first transmission and Raman measurements were taken after just 20 hours of polishing. The resultant pump (514.5 nm) transmission was comparable to the best case using the liquid polish. Polishing continued to 80 hours in the hopes that it would increase the Raman power collected to be comparable to that of the Doko capillary; however, the final measurements for the second capillary ended quite similarly to the first at just 140 counts of nitrogen Raman per second or only 10% as efficient as a similarly sized Doko capillary.

A final attempt was made by returning to the liquid polish to test if additional polishing time could help. The theory tested this time being that the 2 micron abrasive is simply too large to produce a surface that is smooth enough for low losses at visible wavelengths. The polishing was run over the course of a month to bring the final polish time to nearly 350 hours. The pump transmission using the capillary was the highest seen in any of the silver capillary tests and even rivaled the best transmission measurements seen using a Doko capillary. The collected Raman power still did not significantly increase. With the completion of this polishing cycle, alternative means were explored to characterize the final results of the polishing attempts by using a scanning electron microscope (SEM) to examine the surfaces of the polished capillaries.

Prior to the mechanical polishing testing on the sterling tubing, a sample was taken from the end of one of the capillaries as a reference for SEM comparison. The end of the capillary was sanded at an angle to reveal the inside surface and the end was cut off and saved. Following each of initial polishing tests using the liquid polish and the 2 micron cerium oxide, samples were taken from these capillaries to compare against the control sample. In addition to the sterling silver capillaries, a piece of a Doko capillary was split to reveal the silver layer for analysis. Figure 12 shows an SEM image taken of the Doko capillary silver surface. Although there are significant features spread across the internal surface, the vast majority of the silver layer is a smooth, specular surface. Note that the bottom left portion of the image is actually a view of the outside layer of silver that was at one point in contact with the glass frame. The scale of the defects provides an idea of what is acceptable in a waveguide while retaining high Raman efficiency and serves as the goal for any waveguide fabrication technique we would aim to produce.

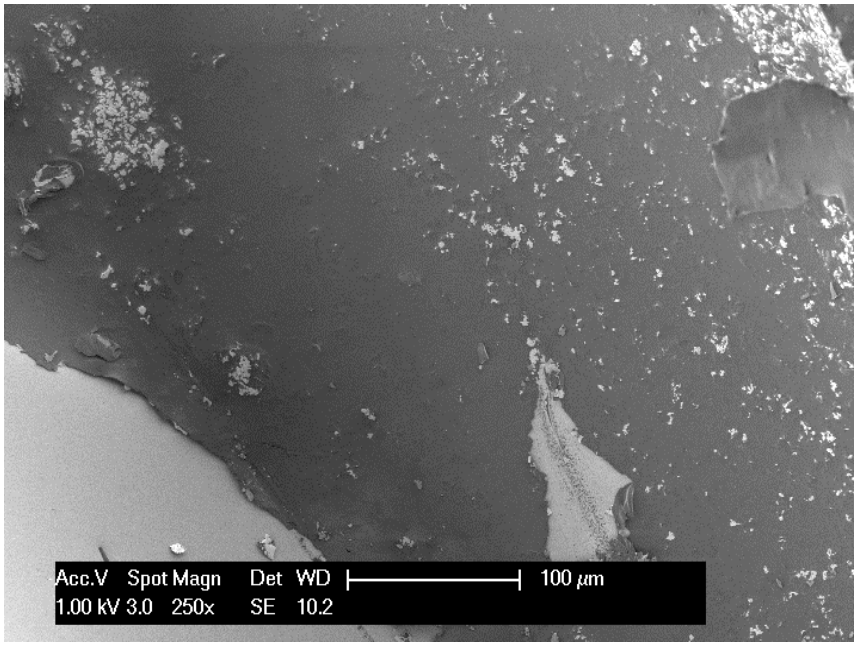

Figure 12 - Doko capillary silver surface

The sterling silver polished capillary samples were examined under SEM as well. A compilation of some of the images is shown in Figure 13. The left images show two different scales of the tube polished using the liquid suspension while the right images show the same scales for a tube polished with the 2 micron cerium oxide particles. Both tubes appear to have significantly rougher surfaces than that of a Doko capillary; however, the tubing polished with the liquid suspension appears to have smaller surface features than those using the 2 micron cerium oxide. The apparent progress made using the liquid suspension encouraged continual testing. Further polishing with the powder abrasive was abandoned as is not sufficient for the surface qualities necessary for multimode wave guiding.

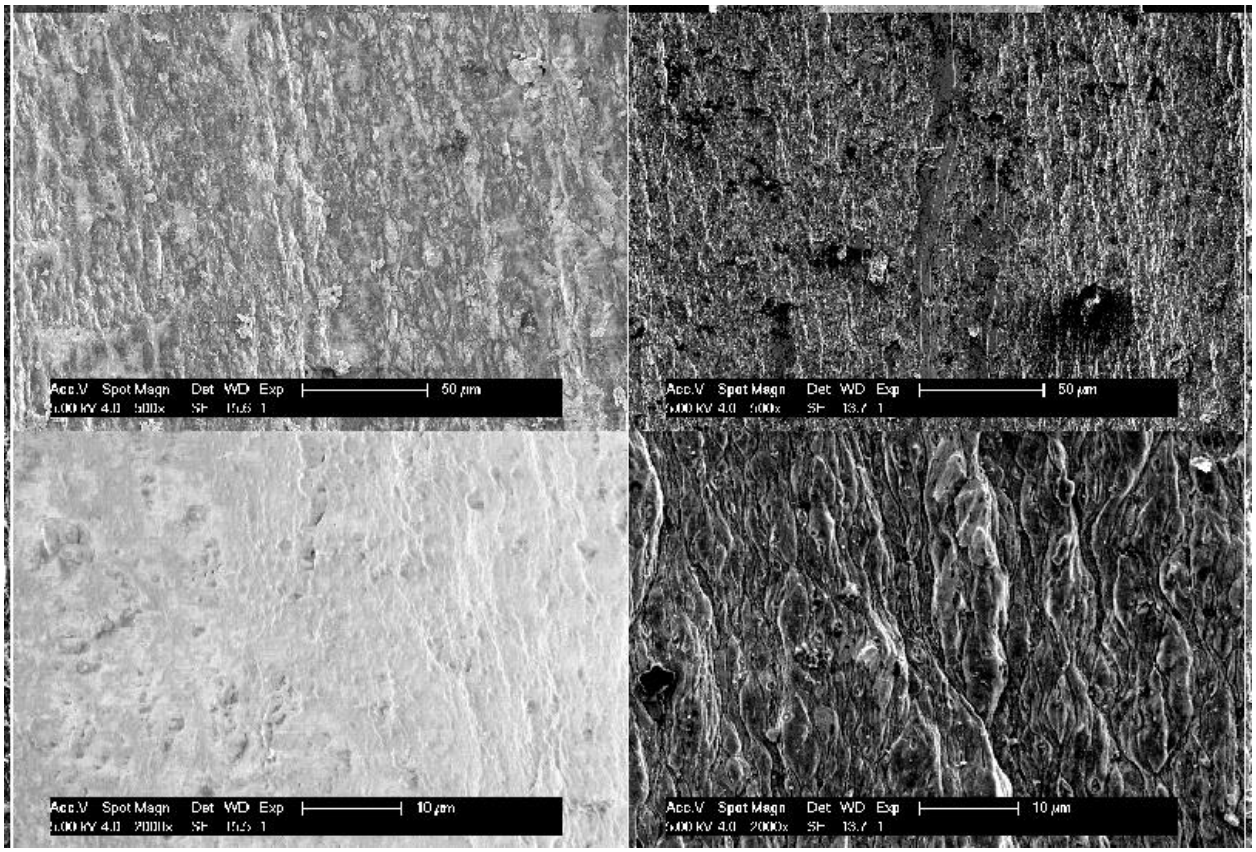

Figure 13 - Sterling silver capillary surface compilation

Initial characterization of the polishing results included pump transmission measurements and Raman throughput. For early results this was sufficient as the first goal in polishing the

capillaries aimed to increase pump transmission to match the Doko capillaries. It was quickly discovered that achieving high pump transmission did not take significant polishing; however, the Raman throughput did not significantly change even with long polish times. An experiment designed to test the relative Raman power throughput was devised using a sharply focused He-Ne laser. This test enables quick quantification of the transmission of high order modes which account for most of the Raman power. The total power transmitted in this configuration indicates the progress of the polishing process. Little to no change in the angular transmission indicated when a particular polishing method reached its useful limit.

To compare the Raman capabilities of a Doko capillary to the sterling silver tubing, the angular transmission measurements were adopted to examine the power transmitted as a function of collection angle. The measurements were taken using a 3.1 mm focal length lens to sharply focus a helium neon laser to excite many modes of the capillaries. Both capillaries were about 30 cm long for an equivalent comparison. The experimental measurements for one such case is shown in Figure 14. These results confirm the limitations of the polished sterling capillaries. Although the sterling tubing is capable of similar pump power transmission, they are still inferior at transmitting the high order modes necessary for efficient Raman power collection. These results explain why the collected Raman power did not significantly change even as the total power transmitted tripled after polishing. Knowing how difficult it is to achieve low losses for the high order modes left us searching for better quality alternatives such as high purity silver tubing.

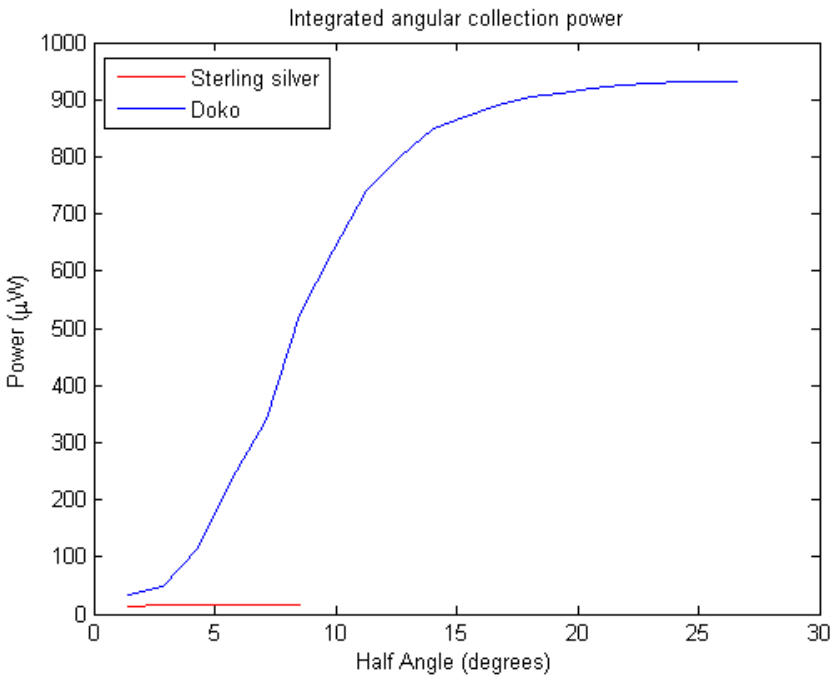

Figure 14 - Integrated angular power transmission

Research grade pure silver tubing was acquired from industrial research supplier Goodfellow to test whether the difference in the material grain accounts for the difficulty in achieving the high specular reflection necessary for low losses of the higher order modes. Based on the experiences with the sterling silver capillaries, the liquid polish was selected to polish the pure silver capillary. The initial state of the capillary was far better than the sterling capillaries readily guiding light even at the longer length of 50 cm compared to the sterling capillary length of just 30 cm.

Following the same procedures as with the sterling capillaries, the pure silver capillary was thoroughly cleaned by first pumping water and methanol through it. In between thorough cleaning cycles were cycles of 5-8 hours of pumping pure liquid polish. This was repeated over the course of a few weeks until the polishing time totaled 40 hours. At this point the capillary was put through multiple cleaning cycles alternating water and methanol pumping. An update of the capillary status was desired. Angular transmission and argon pump transmission

measurements were attempted on the cleaned and dried capillary; however, no transmission was detected in either configuration. No blockages were detectable in the capillary that would prevent light transmission.

The pure silver capillaries selected for this experiment have thin walls and the soft metal does not hold a rigid form. Throughout the polishing process the rigors of placing and removing the capillary from the pump and optical mounts for testing introduced a few noticeable bends. They are obviously detected by rolling the capillary on a flat surface. It is suspected that the loss in light transmission is due to these bends that resulted from handling the capillary. This result is not surprising based on experiences with the sterling silver capillaries. Experimentation with the sterling capillaries showed wildly fluctuating transmission due to the slight changes in the capillary mounting. Bending the capillary in the mount by gently pressing down was sufficient to reduce the transmission to less than 10% of the peak value. These high bending losses are believed to be the same cause of the loss of transmission in the pure silver capillaries indicative of poor reflectivity at non-grazing incidence. The use of pure silver does not provide significantly better results so polishing techniques were abandoned.

The polishing experiments have shown the possibility to turn a low cost sterling silver capillary into a reasonable waveguide for laser transmission with a simple polishing compound and mechanical pump. The application of such a polishing technique for producing waveguides for a Raman sensor however is currently limited. The losses associated with light propagating at higher angles are simply too high to make a waveguide for efficient Raman collection. Transmission must be efficient for half angles as large as 10 degrees to compete with the effectiveness of a Doko metal-lined waveguide.

Throughout the experimentation, one concern was raised that could not be tested with the equipment available, the effect of the flow dynamics in the capillary. The primary factor determining the effectiveness of the polish process is believed to be the nature of how the abrasive interacts with the capillary walls. From the perspective of fluid dynamics, laminar and turbulent flow will determine how aggressively the abrasive will impact the material. Laminar flow is characterized by zero fluid velocity at the tubing walls and high velocity at the center with very little mixing. Turbulent flow is characterized by high fluid turbulence resulting in random mixing as particles flow from one end of the tube to the other [9].

The scattering of the abrasive particles in turbulent flow is believed to be desirable for producing specular surfaces. Characterizing the flow in a tube can be done by finding the Reynold's number for the system. Reynold's number is a dimensionless constant that can be used to quantify the significance of the fluid's inertia and viscosity on the flow. Reynold's number can be found for a hollow tube as

$$R = \frac{QD}{\nu A}$$

where Q is the flow rate, D is the tube's internal diameter, ν is the kinematic viscosity of the liquid, and A is the cross-sectional area of the tube. A high Reynold's number signifies turbulent flow with a transitional range where turbulent flow and laminar flow are observed depending on additional circumstances regarding tube roughness between R= 2,300 and 4,000.

A simple analysis of our pump system using the kinematic viscosity of water, the silver capillary dimensions, and a measured flow rate of about 5.7 mL/min. produces a Reynold's number of just 161. This indicates that the flow within the capillary is laminar for a smooth capillary wall. This would limit the quality of the polish as the abrasive particle's velocity at the capillary walls would be nearly zero. It is possible that the high initial surface roughness

encourages turbulent flow enabling the polishing results observed. As the surface walls are smoothed, the roughness may no longer support turbulent flow and acts as a limiter for polishing. A pump capable of a higher flow rate could produce a turbulent flow within the capillaries even at low surface roughness. Such an experiment may prove to produce capillary walls with sufficient reflectivity to serve as a replacement for the Doko waveguides given enough polishing time to reduce the wall roughness to specular quality.

5.0 CAPILLARY MODE THEORY AND CUTBACK EXPERIMENTS

As part of our interests in maximizing the Raman sensing system's efficiency, a complete understanding of Raman collection in the hollow metal-lined waveguides was necessary. Calculating the mode propagation for the pump light and scattered Raman enables the integration of Raman power for a given waveguide material and dimensions. Such a rigorous numerical analysis provides the means to optimize the waveguide selection for system properties such as collection angle, spectrometer acceptance angle, and pump wavelength.

A theoretical analysis of the losses of propagating modes was performed prior to the experiments to verify the theory described below. A complete explanation of the process is found in [10] although the theory is summarized here as it is relevant to discoveries made during experimentation and alterations made to correct for non-ideal conditions.

Determining the propagating waveguide modes begins with general expressions for the electric and magnetic fields in the hollow core and in the metal cladding and equating the tangential components at the boundary at r = a (Figure 3). This leads to a transcendental characteristic equation that implicitly describes all modes that can propagate in the guiding structure. All fields in the core as well as in the cladding can be written in terms of the longitudinal field components E_z and H_z. The field components in the air core can be described in terms of J_n, Bessel functions of the first kind. These field components can be described in cylindrical coordinates (r, θ, z) as:

$$E_z^i = \sum_n a_n^i J_n(k_i r) e^{i(\gamma z + n\theta)} \qquad H_z^i = \sum_n b_n^i J_n(k_i r) e^{i(\gamma z + n\theta)}$$

where k_i is the (complex) transverse eigenvalue in the core, γ is the (complex) longitudinal eigenvalue, and a_n^i and b_n^i are expansion coefficients. Inside the metal, the E_z and H_z fields can be written in terms of $H_n^{(1)}$, Hankel functions of the first kind:

$$E_z^e = \sum_n a_n^e H_n^{(1)}(k_e r) e^{i(\gamma z + n\theta)} \quad H_z^e = \sum_n b_n^e H_n^{(1)}(k_e r) e^{i(\gamma z + n\theta)}$$

where k_e is the (complex) transverse eigenvalue inside the metal-lining and a_n^e and b_n^e are expansion coefficients. The subscripts i and e denote fields inside the air-core and fields in the metal, respectively. The magnitude of the wave-vector is: $k = \frac{2\pi}{\lambda}$ where λ is the free-space wavelength of the propagating modes. We note that boundary conditions require that the longitudinal propagation constant γ be the same in the core and in the metal.

Equating the tangential components of the electric and magnetic fields at the air-metal boundary produces a set of four continuity equations. The requirement that the determinant of this system of homogeneous linear equations is equal to zero leads to a characteristic equation. For each integer n, there are m solutions to this characteristic equation. Each value of m describes a mode.

The characteristic equation is greatly simplified by noting several physical constraints. Firstly, in this work the only interest is in polarized propagating modes. The experimental objective is to use the capillary to collect Stokes Raman radiation produced by a linearly polarized laser beam interacting with gases with low depolarization ratios. Thus the Stokes Raman light is then also highly polarized, and very little optical power couples into modes that are not linearly polarized. The only set of cylindrical modes which exhibit linear polarization is the hybrid EH_{nm} mode set with n =1. Considering all of the modes in the EH_{1m} set will allow us

to characterize losses in modes propagating at higher angles of incidence, or filling more of the waveguide's angular aperture. Secondly, for the waveguides of interest, the capillary's diameter is large in comparison to the wavelength of the propagating light. Finally, all propagating modes in commercially available silver or aluminum lined capillaries satisfy $\left|\frac{k_{im}}{k_{em}}\right| << 1$; consequently, all terms containing powers of $\frac{k_{im}}{k_{em}}$ that are greater than one can be ignored. These assumptions are more fully discussed in [10] and produce a simplified characteristic equation:

$$J_0(k_{im}a) = \left[\frac{\frac{1}{2}(\nu^2 + 1)}{\sqrt{\nu^2 - \frac{\gamma_m}{k^2}^2}} \cdot \frac{ik_{im}}{k} + \frac{1}{k_{im}a}\left[1 - \frac{\gamma_m}{k}\right] \right] J_1(k_{im}a)$$

The parameter ν is the complex dielectric constant in the metal. This equation can be solved numerically using a perturbation technique. The longitudinal propagation constant (γ_m) is determined from this equation and can be used to find the propagation angle (θ_m) and power-loss coefficient (α_m) for each mode:

$$\theta_m = \cos^{-1}\left(\mathrm{Re}(\frac{\gamma_m}{k})\right) \qquad \alpha_m = 2\,\mathrm{Im}(\gamma_m)$$

An example of this calculation using a 700 μm diameter silver-lined waveguide produces the results shown in Figure 15. In contrast to the closed-form solutions of earlier work that examined this exact problem [11], the calculation here is useful to predict losses for light that travels at large angles to the z axis and accurately predicts the unbounded growth of loss as the propagation angle approaches 90 degrees.

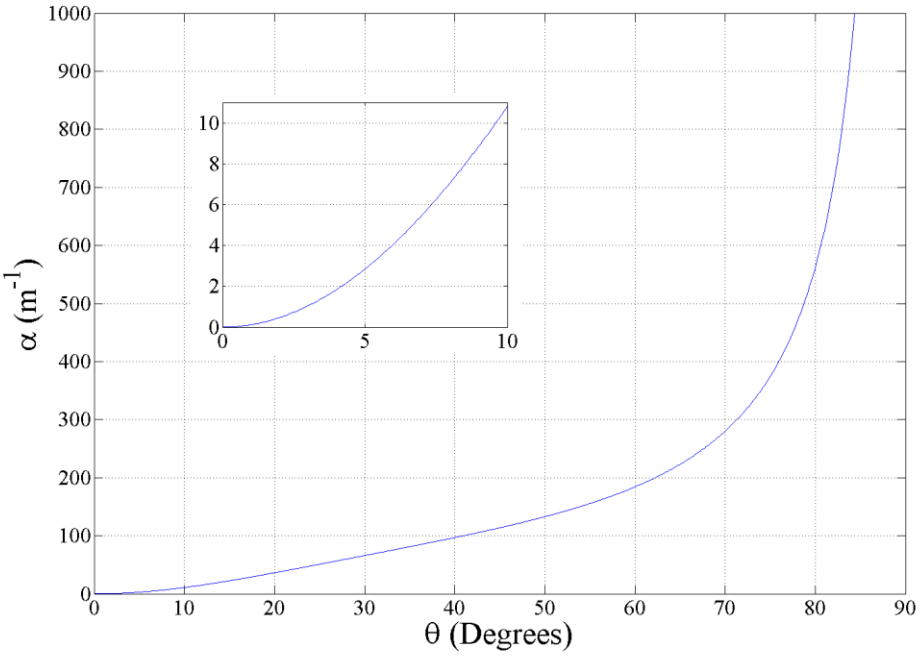

Figure 15 - Simulated loss for all propagating modes in a 700 µm silver-lined waveguide

The aim of the analysis is to accurately predict the backscattered Stokes Raman power, P_S, collected by waveguides of varying dimensions. The loss calculation is extended to this purpose by integrating Raman Stokes power over the waveguide length:

$$P_S = \int_0^{\theta_C} \int_0^{l} 2\pi\sigma\rho P_p \exp^{-\alpha(\theta)z} dz \sin\theta d\theta$$

where σ is the Raman cross section of the scattering medium, ρ is the molecular density, P_p is the pump laser power, l is the capillary length, α(θ) is the Stokes wavelength power-loss coefficient at propagation angle θ and dθ is an increment of linear collection angle. The intent of the calculation is to predict the optimal capillary metal layer and waveguide diameter for given pump characteristics and collection angles. Before the simulations are put to use for designing sensing systems, the accuracy of the calculations is confirmed using a number of experimental comparisons.

The verification of the theory began first with a few simple tests with waveguides of varying length to compare the ratio of collected Raman power for particular configurations. Although these results roughly corresponded with theory, accurate comparisons required a more rigorous experimental method. In order to reduce the number of variables to consider, a cutback experiment was developed. The premise of the method is to perform a single alignment of the system optics and laser with a single long capillary. Data is collected for varying lengths with the minimum error by successively cleaving off a piece of the capillary from the suspended end. This process eliminates any error that would be incurred by realignment of new capillary segments.

The cutback experiments performed to verify the theory all used the same backscattering configuration of Figure 16. The pump laser, the 514.5 nm argon line, is compressed to less than half a millimeter diameter by a 5 to 1 beam compressor. The laser light is coupled to the waveguide by a dichroic beam splitter and focusing lens, BS and L_1 respectively. The beam splitter is highly reflective to the pump light and higher transmissive to longer wavelengths so that it rejects the pump from the spectrometer without interacting with the collected Raman. The capillary is mounted to a nano-positioning stage in a metal flange, Fl. The backscattered Raman is collected and guided by the capillary waveguide and collimated by lens L_1. The Raman passes through the beam splitter and a long pass filter, F, provided for additional pump rejection. The aperture, A, is used in later experiments to control the collection angle. Lens L_2 focuses the Raman to be transferred to the spectrometer by the fiber bundle as described in Section 2. The lenses L_1 and L_2 are separated by the sum of their focal lengths so that the transverse distribution at B_1 is a magnified image of the output of the capillary. The aperture is placed a focal length behind L_1 such that the plane of the light is a Fourier transform of the output of the capillary so

that the aperture size determines the angular collection of the system. Not shown in Figure 16 is the method by which the capillary was suspended to minimize bending losses. The method of suspension varied between experiments and will be covered in the discussion of individual experiments below.

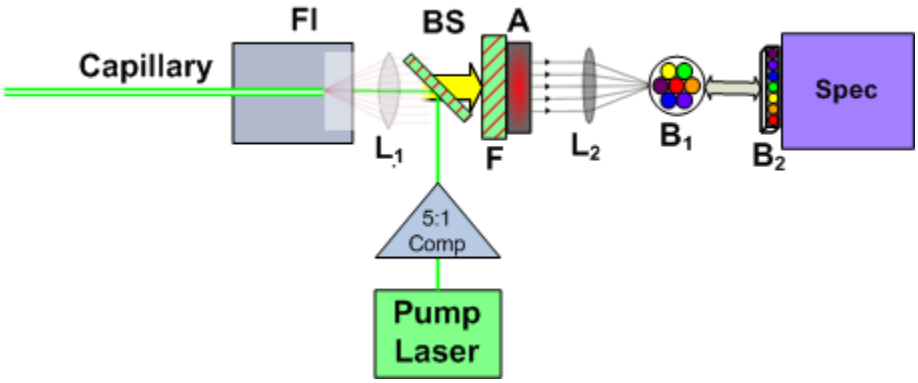

Figure 16 - Cutback experiment backscattering configuration

The first cutback experiment sought to improve the accuracy of the ratios measured in initial tests. For this cutback, L_1 had a focal length of 40 mm, a focal length of 20 mm for L_2, the aperture was excluded, and the capillary was suspended in a spring mount. The mount gripped the capillary firmly at the opposite end while spring provided tension to pull the capillary straight. The capillary selected for the test was initially a 1.8 meter long, 530 µm internal diameter, silver-lined waveguide. The cutbacks consisted of a 30 cm cut followed by a 50 cm cut to bring the final length to 1 meter that served as the baseline power for comparison. The removed pieces were then tested separately as in the initial ratio tests for the sake of comparison.

The ratios of Raman power from the experiment are shown in Table 2. The results clearly show that the theory reasonably matches from the pieces tested as part of a single cutback experiment. The removed pieces suffer from large errors due to the inability to achieve repeatable alignment. The accuracy of the cutback results encouraged the planning of a

complete cutback to test many more lengths and to examine the accuracy of the theory with respect to angular variation.

Table 2 - Cutback experiment Raman ratios

Length	Theoretical ratio	Measured ratio	Percent error
1.8 m	1.19	1.146	3.7%
1.5 m	1.13	1.107	2.0%
1 m	1	1	0
50 cm	0.77	0.455	40.9%
30 cm	0.65	0.556	14.5%

The cutback experimental method was expanded to include the aperture, A, shown in Figure 16 to measure the Raman power as a function of angle as well as length. This modification as well as the decision to use a 700 μm diameter capillary necessitated a change in optics. Lenses L_1 and L_2 were replaced with a 75 mm and a 125 mm lens, respectively. This provided the additional space between the lenses to fit the aperture while maintaining the separation of the sum of the focal lengths. The change in magnification, from 2x to 1.5x, provides for the efficient filling of the fiber bundle input diameter of 1.1 mm. Although the change to the 75 mm lens reduces the angular collection of the optics, the aperture provides the limiting angle. The 0.5 mm graduations between 1 mm and 12 mm diameter provide an effective angular acceptance of 0.4 degrees to 4.6 degrees half angle. The aperture can be removed to expand the collection to the limit of the spectrometer acceptance of f/6.4 or 6.7 degrees half angle with the 1.5x magnification.

The cutback process followed the same steps of the first experiment using the 530 μm diameter capillary only more cuts were taken. The initial length of the capillary was 1.77 m. A 7 cm cut was taken to bring the length to 1.7 m with 10 cm cuts following until only 10 cm

remained. Rather than collecting the total Raman power at the maximum aperture, data was collected for Raman power at 17 different angles to compare the relationship of power against angle. This enabled the ability to compare the relative agreement of the theory by adjusting the measured data by a scaling factor to correct for optical losses and spectrometer efficiency. Figure 17 shows three data sets collected in the experiment demonstrating the relative fit of the experiment to theory. The experimental data is scaled to the simulation point corresponding with 1.7 degrees of the 0.7 m long capillary. You can see that the relative fit between lengths matches quite well. A quick calculation of the scaling constant using the known 44 percent efficiency of the spectrometer and the 90 percent quantum efficiency of the detector indicates these numbers are reasonable within about 20 percent error.

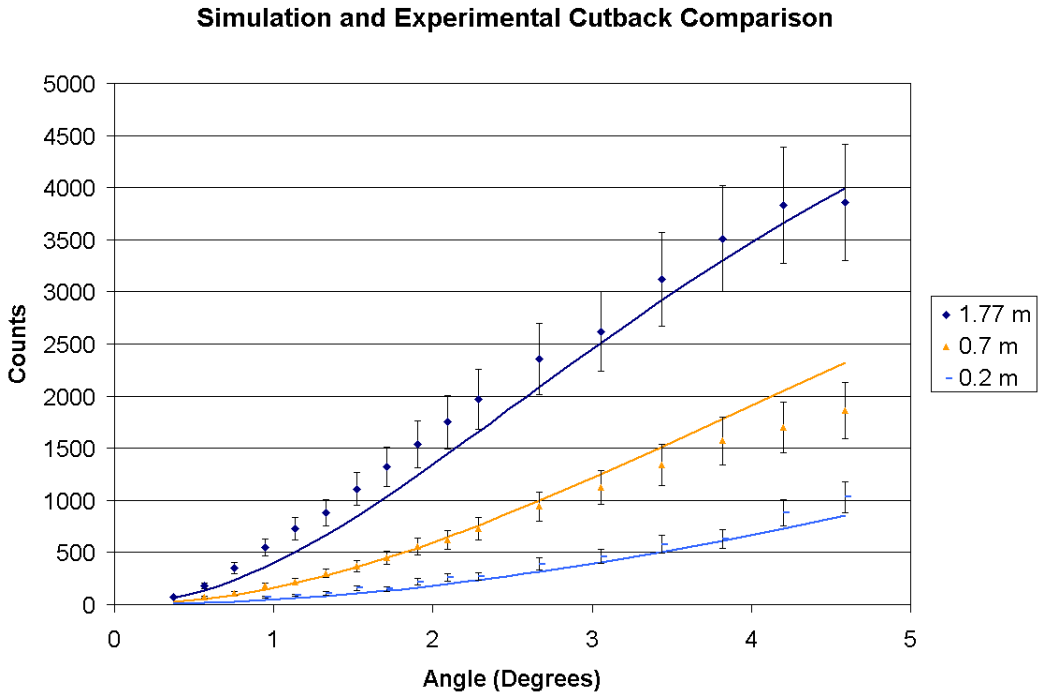

Figure 17 - First 700 µm capillary cutback

The data for the experiment does not fit as closely as desired so error bars were added based on an error analysis that was performed. The analysis looked at the other variables in the

experiment that had not been considered prior to this cutback. Among the problems encountered were laser power fluctuations, transmission changes based on capillary tension applied, and a lack of repeatability using the silicon photodetector for measuring laser power. The results were set aside for a period of time to think through the problem with a new experiment planned at a later date.

When returning to the experiment later, the pitfalls encountered in the earlier cutback experiments were analyzed again in order to reduce the errors to make valid comparisons between all of the collected data. A number of improvements were made to obtain more accurate results with a second set of cutback experiments. These improvements include changes in the experimental equipment to incorporate corrections for other non-ideal behaviors inherent to the system.

The original experiments suspended the capillary using a spring loaded clamp to minimize bending losses. Fluctuations in the transmission and Raman output were discovered when the tension applied to the capillary changed. This observation raised the concern that longer capillaries would experience higher bending losses due to the additional weight. A shorter capillary suspended with equivalent tension would not bend as severely resulting in an error in the measurement as a function of capillary length. To remedy this problem, a metal tray replaced the spring mount for suspending the capillary. The capillary would rest freely in the tray so that it would lay straight regardless of the length. Sections of the tray were removed as necessary as the capillary is cut back in the experiments.

The most significant problem with the earlier experiments actually lies in the accuracy of the data collection. The maximum allowable power density of the silicon photodetector limited some of the measurements. Under the right conditions, the effective detector area was large

enough to avoid saturating the device. It was discovered that careful placement of the detector was required otherwise the effective area on the detector would be too small, the detector would saturate and the reading would reach a maximum. In order to prevent errors in the measurements introduced by detector placement, an alternative detector, designed for high power was selected, as a substitute for more repeatable results. The detector provided consistent data throughout all of the experiments.

Laser power fluctuations were considered following the early experiments. Although the fluctuations account for only a small source of error, a method to correct the measured data was implemented. Operating under the assumption that the input coupling and the waveguide losses would not change significantly over the course of the measurements, the total 514.5 nm power transmitted through the capillary was measured after setup and before Raman measurements were made. The capillary output power was measured throughout data collection and was recorded along with the data. Changes in the measured output power were assumed to result entirely from changes in the laser input power. The data was corrected for these power fluctuations by appropriately scaling each measurement of Stokes power using the 514.5 nm output power measurements. Comparing individual data points is done by converting the recorded data to a ratio of the Raman power to pump power, P_{Raman}/P_{Pump}.

A puzzling discrepancy in the original cutback experiments involved the errors between long and short capillaries. No matter how the measured data was scaled, there was always an error that was a function of capillary length. The error was small enough that it did not draw attention until repeating the experiments with the other error corrective changes implemented. Since the simulations of the Raman theory were based entirely on the Raman scattered and collected in the waveguide, there is an error introduced in the experimental data resulting from

Raman that is scattered and collected in free space since the nitrogen Raman line (2331 cm^{-1}) in air was selected for the experiments. The free space Raman is measured by removing the capillary after the primary measurements are performed. This data set is subtracted from data collected for each length in order to show only the contribution of Raman collected by the waveguide itself.

A similar error affects the data as a function of length in the form of pump losses. Generally, the pump losses in the Doko capillaries are low enough to ignore for the purposes of the comparison with theory. In one particular experiment however, the pump losses contributed to a significant deviation from theory as the capillary was reduced to the shorter lengths. These losses are easy to account for in the simulation of the total collected Raman power by adding an additional loss term, α_p:

$$P_S = \int_0^{\theta_C} \int_0^{l} 2\pi\sigma p P_p \exp\left[-(\alpha_p + \alpha(\theta))z\right] dz \sin\theta d\theta$$

The final change to reduce measurement error was also the simplest to implement. All collected data was performed at the longest integration time possible for the peak point of the data set. Using a longer integration time reduces error introduced by the random dark and readout noise. The average background noise level is subtracted to extract an accurate measurement of the Raman. The use of the silver colloidal paint to reduce fluorescence emission, as discussed in Section 3, also served to maximize the accuracy of the Raman count for each measurement.

Following the implementation of the corrections for the previous experiments' errors, another 700 μm diameter silver-lined capillary was cutback to produce better results. The experimental configuration was the same as the previous trial with a 700 μm capillary only using

a 30 second integration time as opposed to the 3 second integration time used previously. The resulting data is shown in Figure 18. The data shown includes an additional correction for pump power loss of 0.275 m^{-1} due to surface imperfections as described above. This correction combined with the normalization of collected power to input power provides a fair fit. The simulated data has been scaled so that it agrees with the measured data at one point (l=50 cm, θ_c = 2.3 degrees). This normalization accounts for detection efficiency.

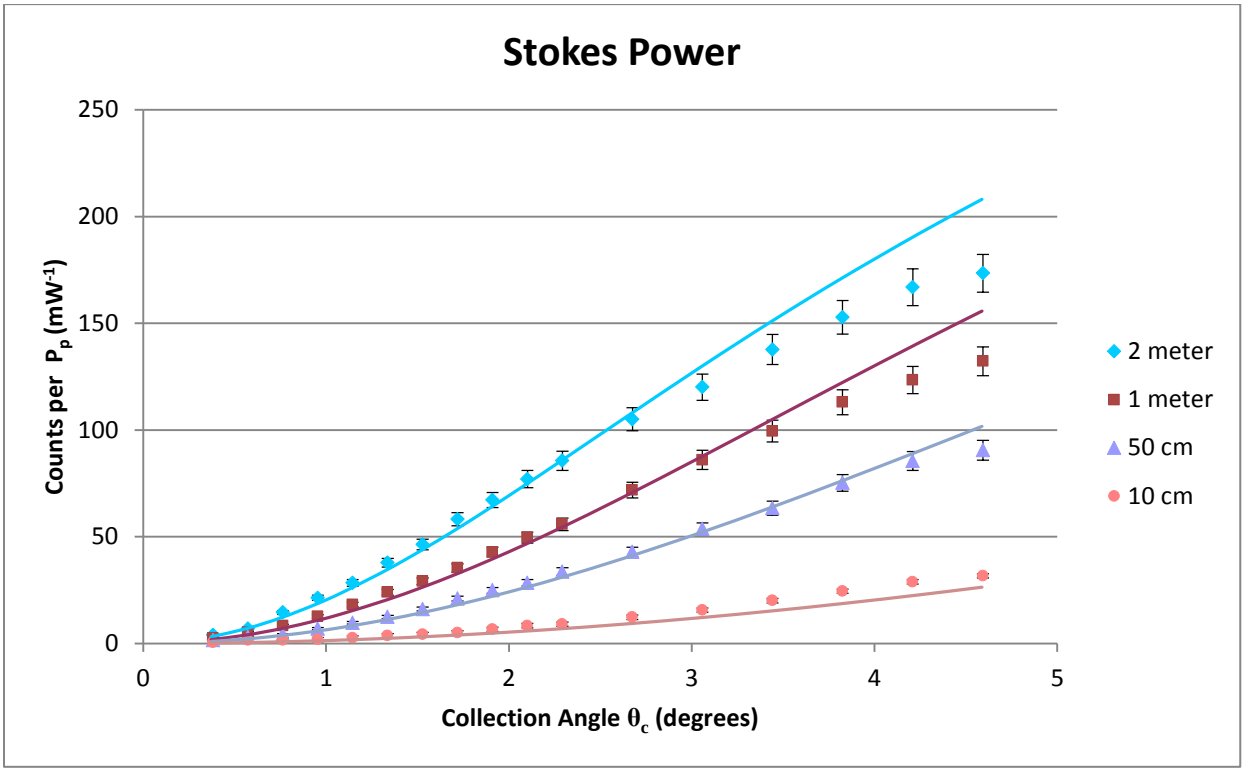

Figure 18 - Retrial of the 700 µm capillary cutback

The capillary used in this experiment differed from the others used previously. Light leakage along the length of the capillary was not uniform. A number of obvious voids in the silver lining allowed additional pump light to leak out. Although the data matches exceptionally well at the lower collection angles, the significant surface imperfections found in the capillary used in this particular cutback result in deviations from theory at the higher angles and longer

lengths. In addition to this deviation, the pump power was significantly attenuated. The measured pump power loss coefficient was 0.275 m^{-1} or about an order of magnitude larger than the simulation predicts under the approximation that the pump only excites the first few modes. These losses contributed to the error in the relative Raman power collected at each length. Even though the simulation was modified to account for this additional loss, a waveguide without the surface imperfections was desired for a proper comparison with waveguides of other sizes and materials. For this reason the experiment was repeated with one last 700 μm diameter silver capillary.

The last experiment followed the same procedure as the previous cases with one exception. The aperture that provides the limit of collection angle (see Figure 16) was removed to collect an additional data point at 6.7 degrees collection angle. The measure 514.5 nm transmission losses were negligible so the α_p term in the simulation was removed. The resulting data is plotted in Figure 19. Note that although the y-axes of Figure 18 and Figure 19 are similar in magnitude, the lower losses of the replacement waveguide and the addition of the extra data point required a reduction in the experimental integration time to 10 seconds to avoid saturation of the detection system. The resulting data matches well even at the largest collection angle measured in this experiment demonstrating the theory is accurate. Note that in this experiment the data was scaled to match the simulation at 4.6 degrees for the 1 meter long capillary

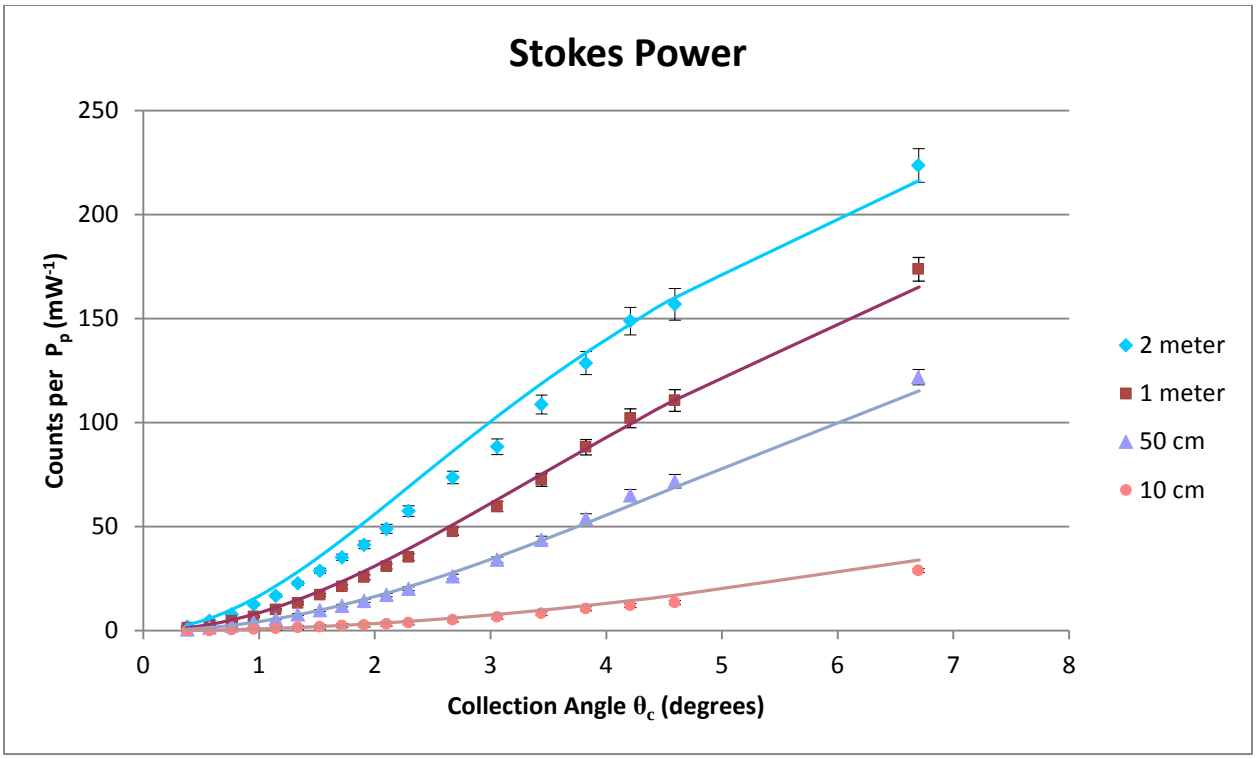

Figure 19 - Final 700 µm cutback results. Solid lines are from the numerical simulation.

In an effort to provide a comparison with another capillary material, a 700 µm diameter aluminum-lined capillary waveguide, also by Doko Engineering, was selected for another cutback experiment. Using the same diameter provides the advantage of using the same optical configuration as the previous cutback. Additionally, the expected coupling loss is similar resulting in an accurate comparison. The resulting measurements using the same procedures for the aluminum capillary are shown in Figure 20. The two shorter lengths show a good match with theory even considering experimental error; however, the longest segment presented a significant deviation from the theory. The deviation was noted before performing the cutback and numerous attempts were made at identifying a source.

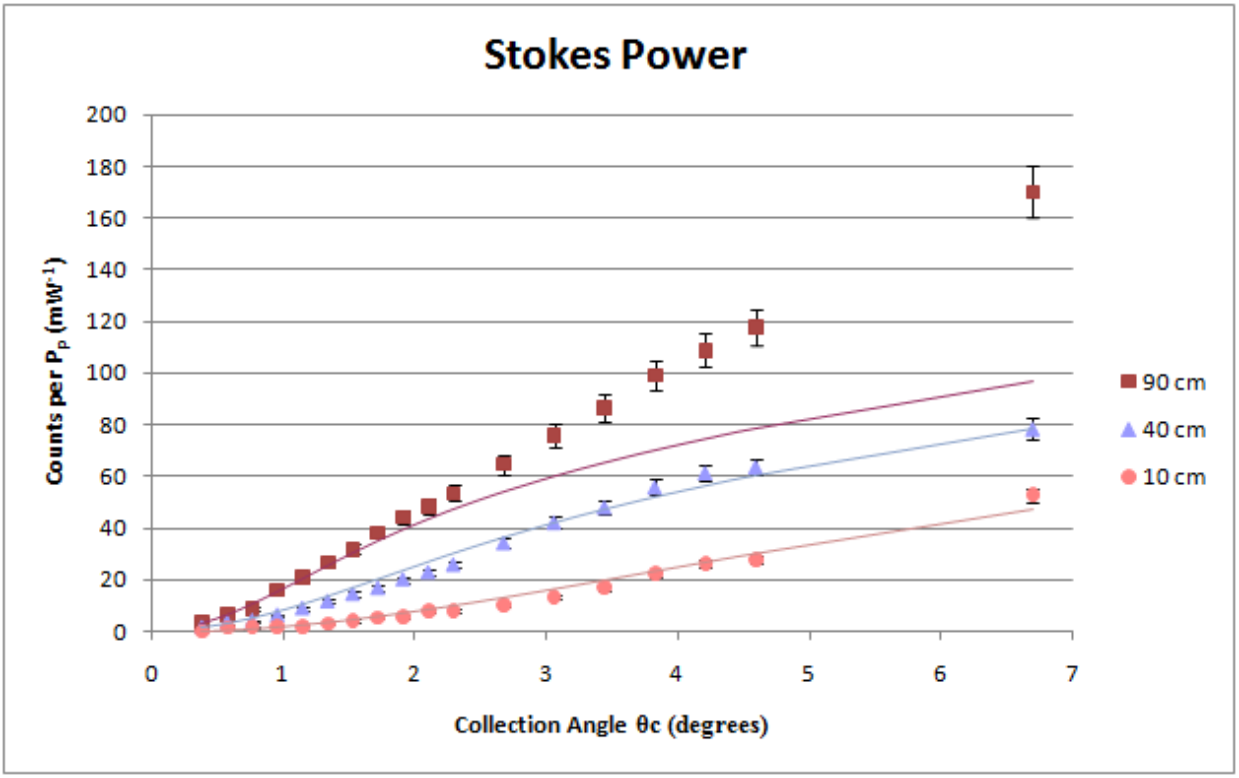

Figure 20 - 700 µm aluminum capillary cutback

After completing the cutback experiment the 50 cm segment that was removed as part of the first cut was tested independently. The resulting data was plotted to compare it to the remaining data in Figure 21. Although the segment is 10 cm longer, the expected relative power is only 6 percent higher than the 40 cm segment at the 6.7 degree collection angle. The results show that the collected Raman power is significantly higher than expected indicating that the discrepancy is restricted to that section of capillary. The aluminum capillaries, unlike the silver coated variant, have no polymer coating to protect the metal layer. Only a thin oxide layer is expected to form on the metal lining. The results indicate some disturbance may have resulted in a thickening of the oxide layer that would enable it to interact with the guiding waves to increase reflectivity at the higher angles. Due to the inability to accurately characterize this effect on the

capillary and the belief that the deviation does not impact the other measurements, the data collected for the 90 cm segment is not used in the comparison with the silver cutback results.

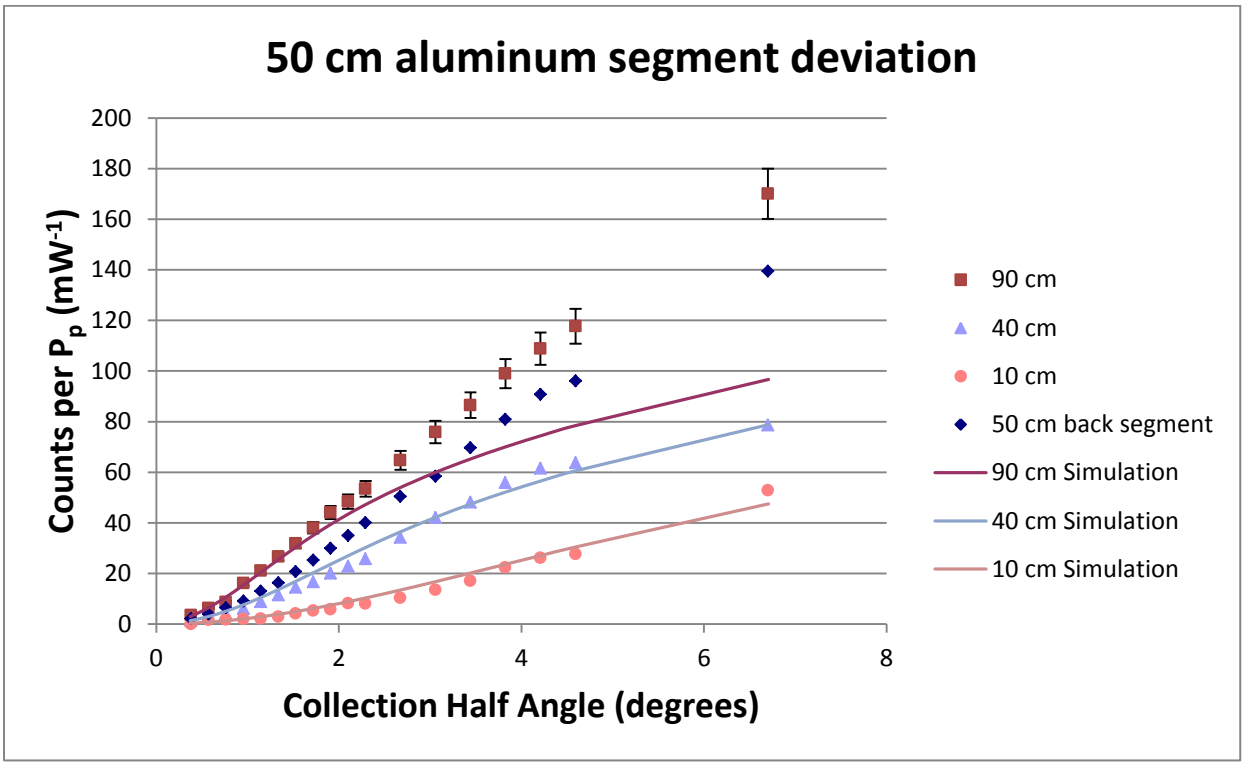

Figure 21 - Analysis of the anomalous capillary segment

An additional comparison was considered using a 320 µm diameter silver-lined capillary. A challenge was presented by this idea in that the coupling associated with the smaller dimensions would not allow a proper comparison of the results. The narrower guide suffers from significant coupling loss using the available beam telescope such that a replacement would be required to achieve losses suitable for comparison. A set of data collected with the full length of capillary revealed that the variation of Raman power with collection angle appeared to follow theory. The magnitude of Raman power did not reflect theory when comparing the data against the larger diameter waveguide cutback experiments due to the additional coupling losses seen in the 320 µm diameter capillary.

The final comparison used to confirm the theory is shown by graphing the data from the two cutback experiments as in Figure 22. Note that in this case all of the data sets, including the aluminum segments, are scaled to the 1 meter long silver-lined capillary at 4.6 degrees as done with the silver-lined capillary alone in Figure 19. Note that the aluminum data was collected with a 30 second integration time. The data collected for the silver capillary was multiplied by three to normalize the data to equivalent collection times. The data matches the theory even when comparing the data across capillary materials suggesting that the theory as implemented is accurate with respect to these changes. This confirmation allows the simulations to extend to other waveguide materials with confidence in the output.

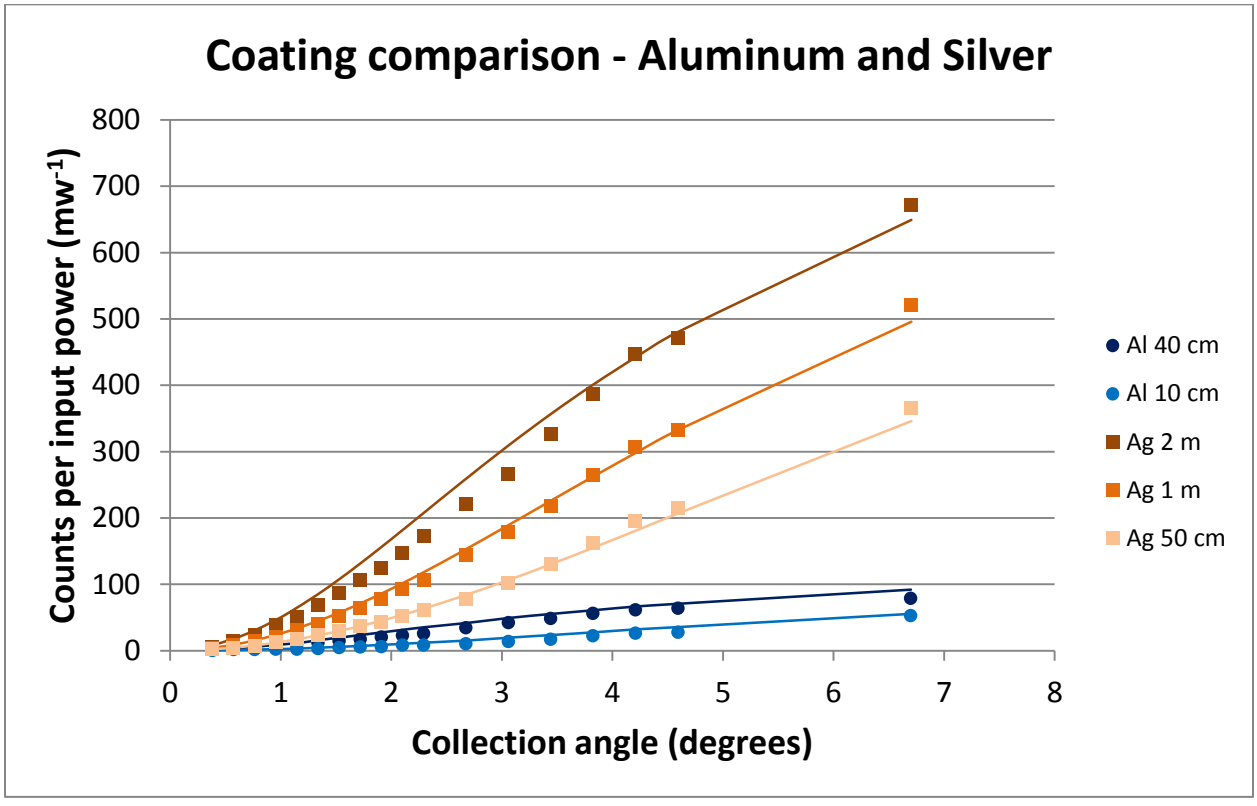

Figure 22 - Waveguide Raman collection cross comparison

6.0 ROTATING FILTER SPECTROMETER

Among the primary goals of the rotating filter spectrometer reported here is the minimization of cost of the complete Raman sensing system. Producing a low price system began by investigating the replacement of the expensive waveguide with a low cost alternative as discussed in Section 4. The largest cost of the system however is the spectrometer and CCD array detector accounting for half of the total price of the complete system. A suitable replacement would enable the technology to rapidly penetrate the market by offering a much lower cost alternative to the current technologies while offering greater detection capabilities. Accomplishing this task required a method to discriminate individual signals for detection and measurement. The use of tunable optical filters to provide the spectral selectivity necessary to isolate individual Raman peaks was explored to accomplish this task.

The introduction of the VersaChrome tunable bandpass filter by Semrock enables consistent pass band response over a 70 nm tunable range [12]. Tuning is accomplished by rotation of the filter to vary the angle of incidence upon the filter. This is possible with both the VersaChrome filters as well as with narrow-band fluorescence filters. Although the VersaChrome filters are specifically designed for this purpose, fluorescence filters have a narrow range over which they can be tuned with little distortion and are used in some experiments for their narrow bandwidths. One VersaChrome filter is sufficient to isolate the majority of the Raman lines of interest. With the filter providing wavelength discrimination, a simple silicon

photodetector provides signal power measurement. The introduction of a second filter allows for reduced effective bandwidths for greater selectivity. The complete implementation of the rotating filters is presented in Figure 23. The system features a beam splitter, BS, to couple the pump light into the capillary through lens L_1, the captured Raman passes through the beam splitter and pump rejection long pass filter, F, an aperture, A, and the lens L_2 focuses the signal on the silicon detector. The tunable filters, TF, are mounted on a rotating platform with an adjustable angle, θ, between the filters to tune the composite bandwidth. The offset in angle results in an overlap of the two passbands to produce a narrower passband although at reduced transmission. The aperture was added as a result of the discovery that the tunable filters would otherwise limit the aperture as a function of angle. This discovery and its implications are discussed in more detail later in the section.

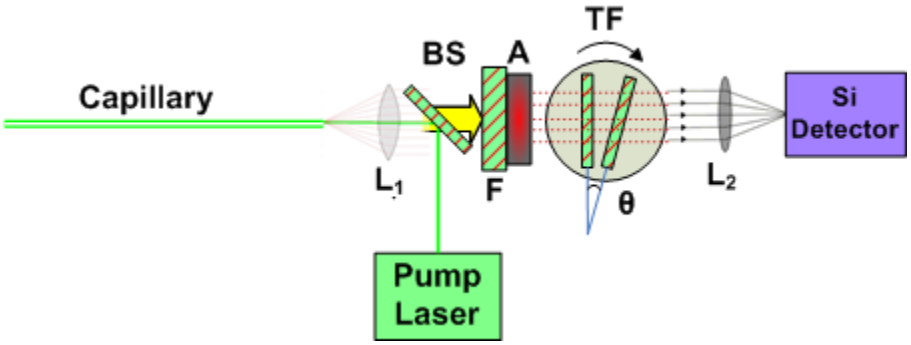

Figure 23 - Rotating filter spectrometer system

The investigation of the use of the filters in building a replacement spectrometer began by analyzing the spectral response of the tunable filters. The filter response was tested at a number of angles to verify the angular and transmission response. A plot using a single filter and the dual filter configuration is shown in Figure 24. The spectral content of the white light source used in this experiment is also shown. The transmission bandwidth of a single filter is nearly constant over its designated operating range, only dropping off past the 60 degree tuning limit.

Figure 24 also shows the transmitted intensity though a pair of filters. The second filter in the dual filter configuration is tuned approximately 10 degrees from the primary filter.

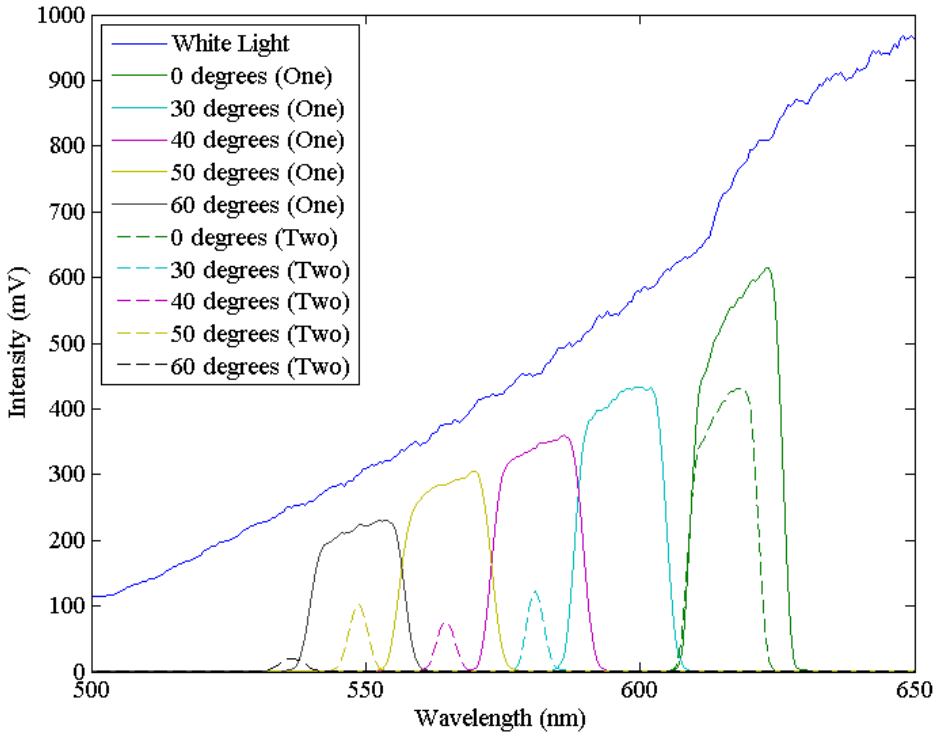

Figure 24 - Response of single and dual filter configuration at various tuning angles

These results show an undesirable consequence of the nonlinear shift of the dual filters' center wavelength with angle. Near normal incidence, the filter's center wavelength does not change as significantly with angle as it does at higher angles of incidence, as shown in Figure 25, so the bandwidth of the dual filter arrangement varies as a function of tuning angle. This limitation affects the amount of fluorescence or other optical noise collected. By using the known bandwidth and center wavelength of the filter as a function of angle, the effective bandwidth of the pair of filters is graphed in Figure 26. The figure shows ten cases with 1 to 10 degrees angular separation between the filters starting from the top. The greater the angle between the filters the narrower the resulting passband; however, the significance of the

nonlinear center wavelength shift increases so the bandwidth changes more significantly with angle. Figure 26 shows this effect in that the larger angular separation exhibits a sharper change in bandwidth over the tunable range thus there is a tradeoff between a narrow passband and a stable effective bandwidth in the two filter configuration.

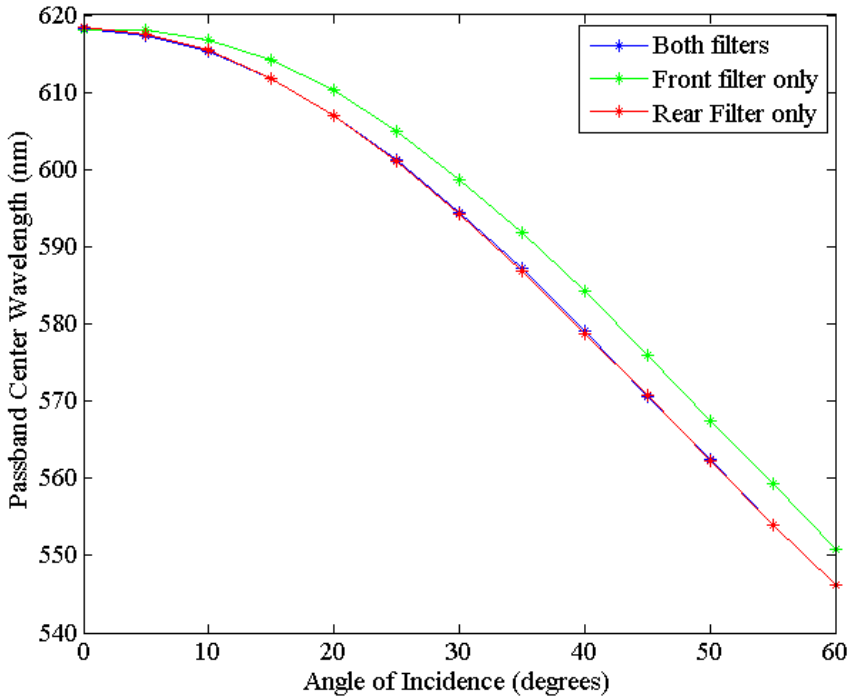

Figure 25 - Tunable filter center wavelength response experimental observation with 10 degrees between the filters in the filter pair.

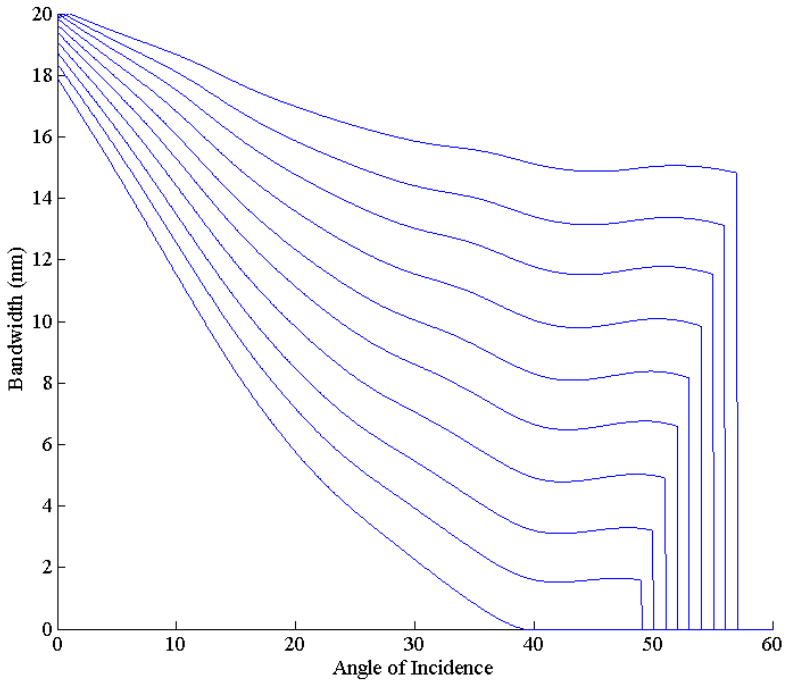

Figure 26 - Effective bandwidth variation for the dual filter configuration

Our early studies of the filters as a means to detect and measure Raman explored the relative strength of the signals as detected in complete spectra. Figure 27 shows one such spectrum captured by a silicon detector by rotating a single filter. The spectrum is recorded by rotating the filter from a starting angle of 60 degrees, or a center wavelength of 550 nm, to 0 degrees angle of incidence, or center wavelength 620 nm. Note that the mapping of angle of incidence to wavelength is nonlinear as a result of the nonlinear shift in center wavelength of the filter pass band. The dashed line marks the location of the nitrogen Raman peak, 574.5 nm, which appears distributed over a 20 nm range as a result of the convolution with the filter pass band. Although we expect the noise levels to trend to higher levels at higher wavelengths due to fluorescence, a significant drop in the measurement below 560 nm demonstrates the effect of the reduced aperture of the sharply angled filter. The 35 mm wide filter only provides the full 1 inch aperture to match the remaining optics when the tuned angle is less than 45 degrees.

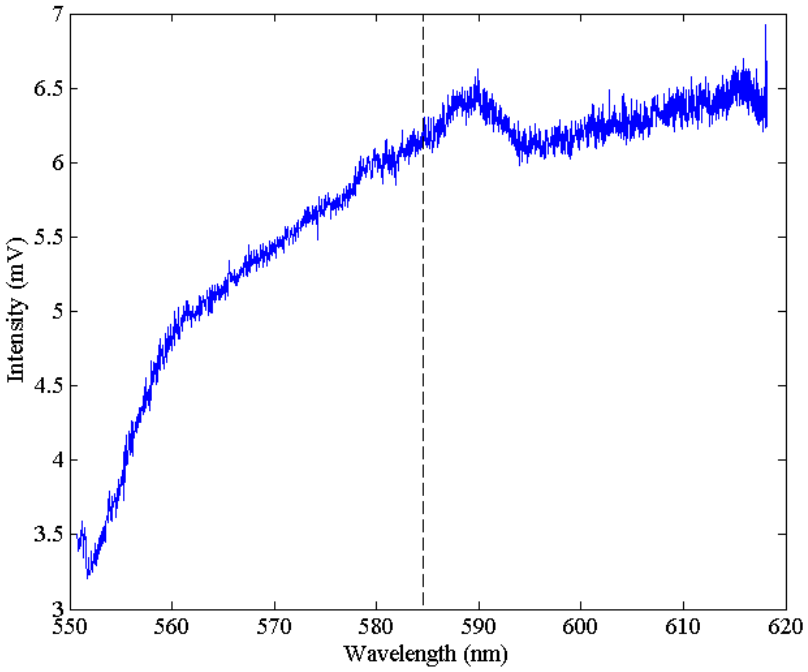

Figure 27 - Example spectrum captured by a silicon detector with a rotating filter

The wide bandwidth of the filter allows a significant amount of fluorescence to pass overwhelming the small Raman signal. Combined with this problem is the high noise associated with the large, 5 mm^2 area, silicon detector. Extracting a meaningful result from the spectra proved difficult. The idea of applying a deconvolution using the known filter passband profile was investigated as a way to isolate the Raman from the noise. The numeric instability of deconvolution algorithms in the presence of noise produced unreliable output. Similar challenges are faced using two tunable filters. Although the composite passband using two filters is narrower resulting in lower noise levels, the bandwidth of the composite system changes significantly with angle. The change in bandwidth provides an additional challenge as the captured noise varies for different wavelengths. For these reasons, the use of the tunable filters for producing scanned spectra was abandoned for a more direct approach in measuring Raman

signals. This was done by shifting the focus to only measuring the Raman peaks as opposed to capturing full spectra.

Measuring the Raman peaks alone is accomplished by using the sharp transition of the passband edge to modulate the Raman signal. This technique rejects the additional noise capture in the wide passband. This concept has its origins in wavelength modulation absorption spectroscopy (WMS) where the pump laser wavelength is varied to induce a sinusoidal response in the measured signal [13]. A change in the pump wavelength in absorption-WMS near the absorption wavelength produces measurable harmonics of the modulation frequency *f*. A similar idea can be applied using the filter band edge to modulate the signal. The filter is tuned to place the band edge at the Raman wavelength. The sinusoidal rotation of the filter will tune the band edge modulating the transmitted Raman signal. Figure 28 shows the spectrum of the collected light from the two extreme ends of the tunable filter in a 1.5 degree sinusoidal rotational cycle. The two curves capture the case where the filter is tuned to longer wavelengths rejecting the methane Raman peak and the shorter wavelengths where the filter collects the Raman-scattered light. The small change in the pass band does not significantly affect the collected fluorescence noise while the Raman is modulated and changes by about a factor of four as the filter is rotated. The placement of the filter is an important consideration in using this technique. As before, at high angles of incidence the effective aperture of the filter is reduced, resulting in the introduction of a sinusoidal component of detector output due to fluorescence noise.

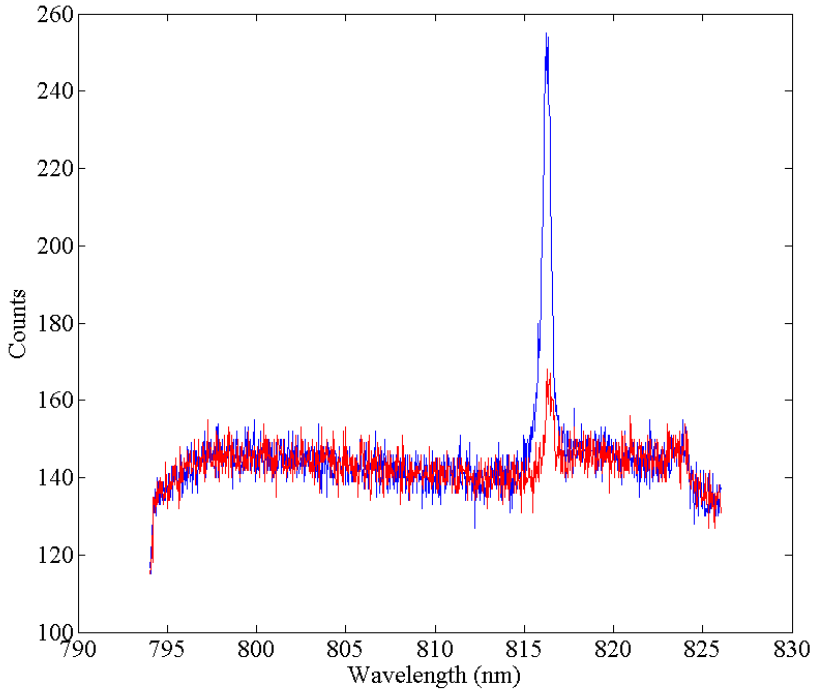

Figure 28 - Relative peak from a sinusoidal rotation of the tunable filter

The rotational scan on the Raman peak produces a sinusoidal signal with amplitude proportional to the concentration of the measured gas. A lock-in amplifier following this signal could provide a direct measure of the gas concentration. A time-domain plot of the optical response of the rotating filter is shown in Figure 29. The sinusoidal component from nitrogen Raman is clearly visible for the first 50 seconds of the measurement. When the filter is then rotated off the line the sinusoidal component disappears indicating little to no fluorescence noise contributes to the measured component at frequency *f*.

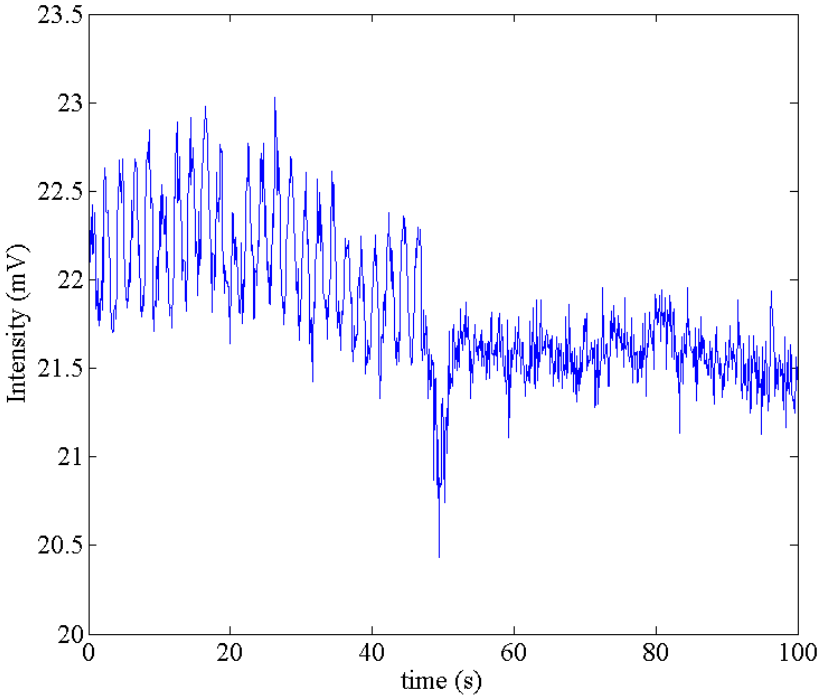

Figure 29 - Temporal rotational measurement showing no off-peak noise

Measurements without a sinusoidal component in the absence of a Raman line are not common across all test cases however. Many cases tested using a combination of the argon (514.5 nm) and diode laser (660 nm) pump and the nitrogen Raman and methane Raman lines indicated this technique is still quite vulnerable to noise even with the reduced fluorescence noise using the longer pump wavelength (660 nm). The increased fluorescence near the nitrogen Raman line increased its sensitivity to noise thus requiring smaller rotational spans to avoid introduction of significant noise. An additional contribution to the sinusoidal component includes pass band deformation in the case of the two-filter composite configuration and with fluorescence filters at high angles. The widening of the composite band pass using two VersaChrome filters near normal incidence limits the use of this configuration as a potential means to limit captured noise. A narrow passband fluorescence filter was tested to determine how such a filter would serve as a replacement for the VersaChrome as many more wavelength

options are available. The fluorescence filter experiences significant passband deformation at high angles of incidence effectively limiting the noise-free tunable range.

Capturing enough data points to reproduce the sinusoidal signal at a fast speed requires the reduction in collection time for individual points. The smaller collection times increase the significance of detector noise with respect to the Raman signal. The 2.5 mm diameter silicon detector used for collection up to this point was determined to be too large as the noise levels are often as strong as the Raman signal. To reduce the noise levels, the CCD array was used as a low noise detector by operating the spectrometer grating in zero-order while taking just one column as the measured data. For an end use system, the CCD array and spectrometer would be replaced by an ultra-low noise silicon detector. The substitution of the CCD array vastly improved the results of the experiments as in Figure 30. Here we see a clear sinusoidal component for 100 psi methane compared to the same measurement taken under vacuum. This case uses a single fluorescence filter with a 1.5 degree angular sweep and a 660 nm pump. The filter was tuned so that Raman line was set at the center of the longer wavelength band edge.

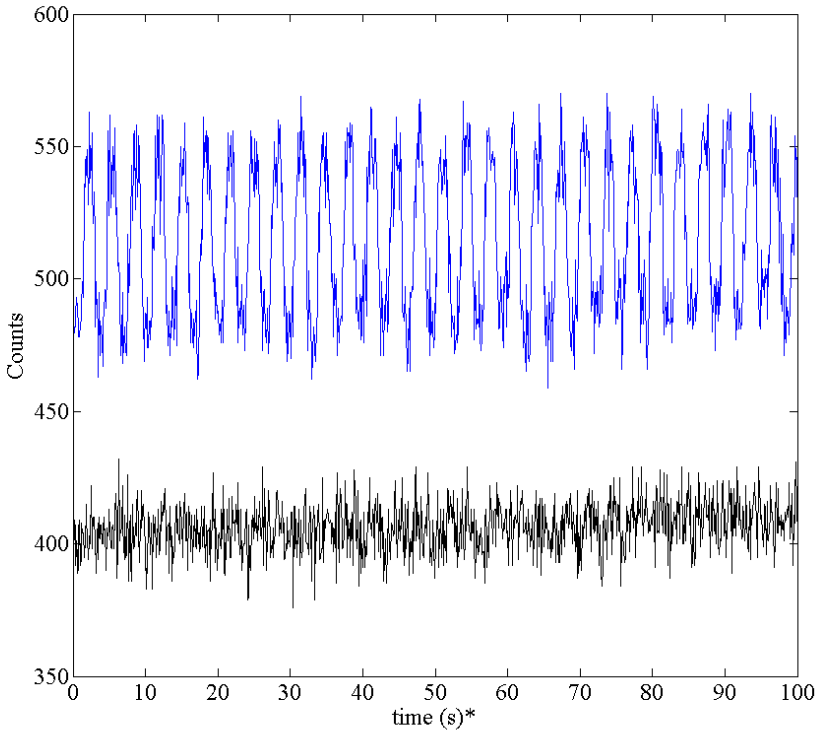

Figure 30 - CCD captured rotational scan with methane (top) and vacuum (bottom)

Taking the Fourier transform (using Matlab) of the data graphed in Figure 30 produces the results shown in Figure 31. The low noise level available using the CCD array as a detector reveals that even under vacuum, a small component appears at the rotational frequency *f*, corresponding to an index of 32. It is this result that inspired the further investigation of the principles of WMS. The maximization of the second harmonic is common in WMS by modulating the tuned wavelength sinusoidally around the center of the absorption line to generate a signal at 2*f* [13]. A similar procedure was explored for use with the Raman system using the tunable filters after witnessing the higher harmonics in numerous scans.

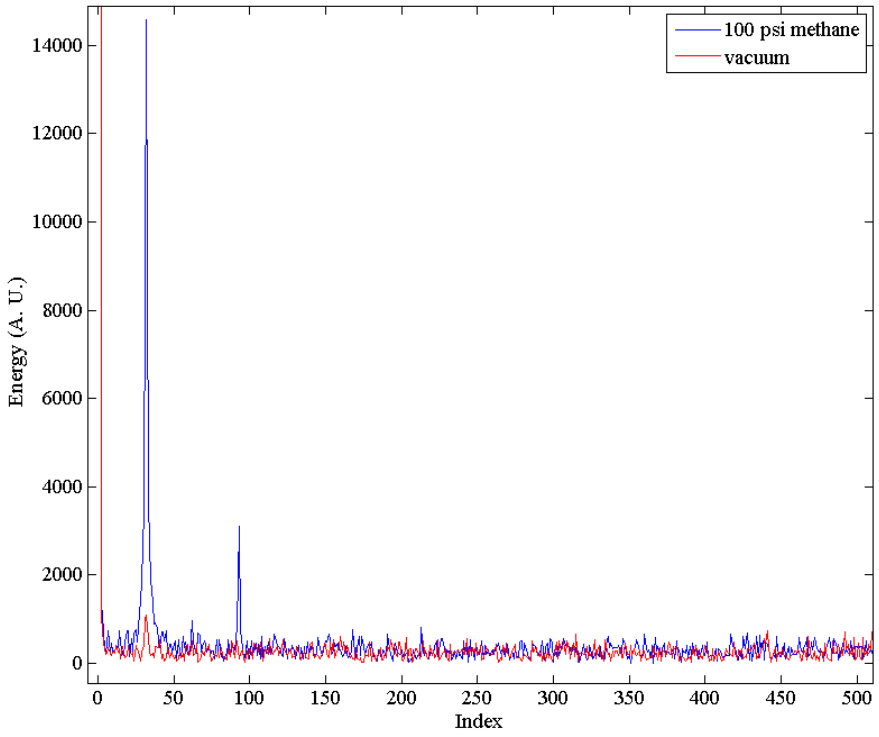

Figure 31 - Fourier transform of the signal captured on the CCD

Second harmonic generation in absorption WMS is accomplished by tuning the laser wavelength sinusoidally around the absorption peak of the line of interest. In the tunable filter Raman system, this is equivalent to tuning the entire filter bandpass across the Raman peak. The advantage of this technique is that the noise and filter band shape distortions only contribute to the signal at frequency *f*. Such a benefit enables both single filter and dual filter configurations to function with no induced noise in the observed second harmonic signal.

One means to accomplish the second harmonic measurement is to use the composite filter pair to produce a narrow effective bandpass. Figure 32 shows the effective filter profile for the paired configuration. The filter shape is visible as a result of the wide band fluorescence noise. The fluorescence noise decreases monotonically over the small spectral windows measured in the experiments so it is not expected to contribute to the 2*f* signal. The Raman peak on the other

hand, is situated at the center of the passband so it will contribute to the 2*f* signal as the filters are rotated sinusoidally around this set point. The data shown in Figure 33 is collected using the CCD in with the grating set in zero order as the filter is rotated sinusoidally; it shows signs of a second harmonic when rotating around the nitrogen peak when the capillary is filled with air and no second harmonic when the capillary is under vacuum.

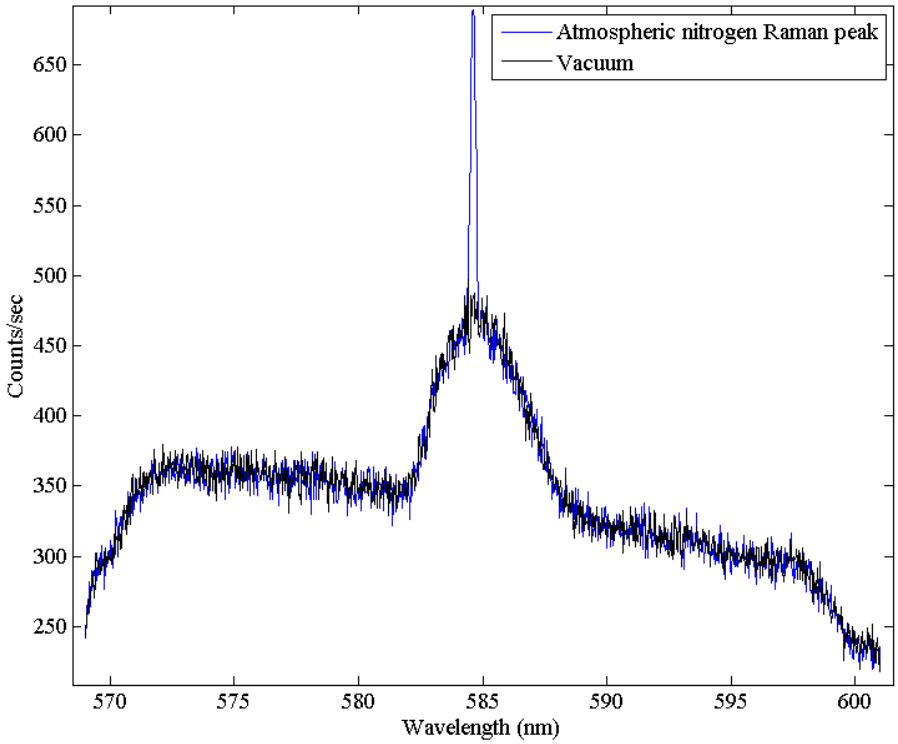

Figure 32 - Filter pair effective bandpass for second harmonic generation

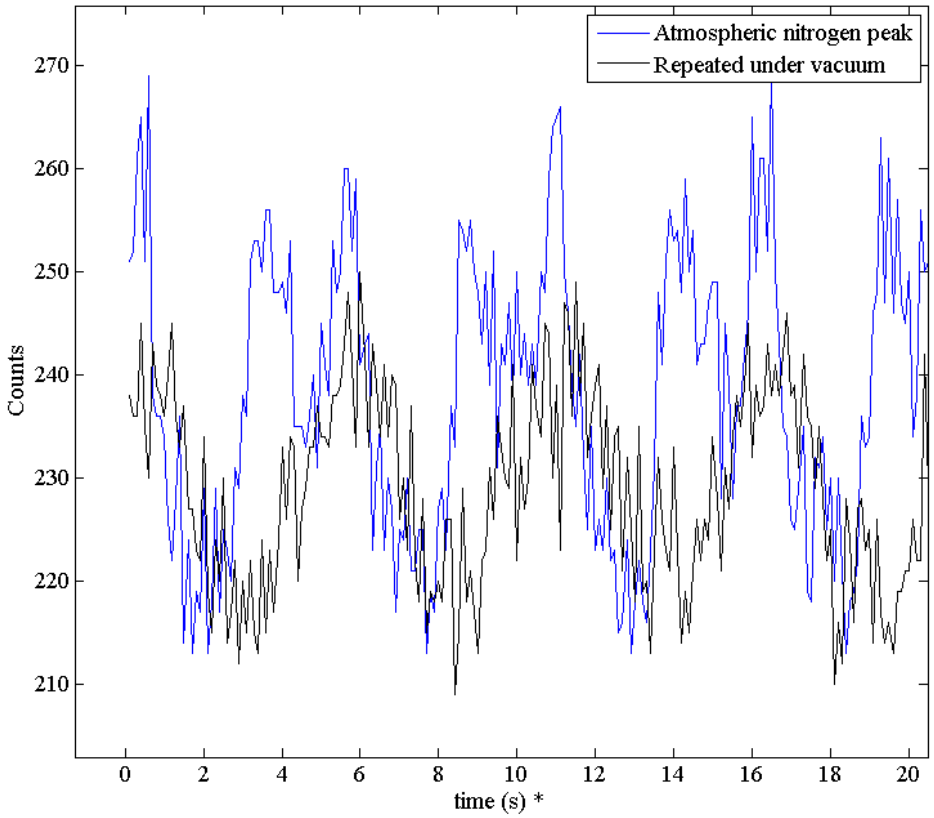

Figure 33 - Time domain collection using the VersaChrome filter pair

Analyzing the data to find the signal to noise ratio is done by taking the Fourier transform of the measurements as done in the previous experiments. In addition to the two test cases shown in Figure 33, the experiment was repeated with the filter pair's tuned center wavelength set to reject the nitrogen Raman line to demonstrate that no other effect from the gas was influencing the results. Figure 34 shows the FFT of each of the three cases and as expected the second harmonic, located at index 37, is only above background noise levels when the filters are centered on the nitrogen Raman peak.

Note that the fundamental frequency f experiences significant noise in all three configurations in contrast to the previous experiments using one edge of the filter passband. This noise is readily apparent in these experiments largely due to the greater rotational span used in

these measurements. The previous experiments typically rotated with less than 1 degree amplitude of rotation corresponding to less than 1 nm wavelength shift as this was sufficient to span the linear portion of the band edge. The experiments performed here require 3 degrees of rotational amplitude to fully utilize the 3 nm wide passband to generate a strong second harmonic. This result highlights the stability of using the second harmonic for accurate sensing versus the single edge, fundamental frequency scanning.

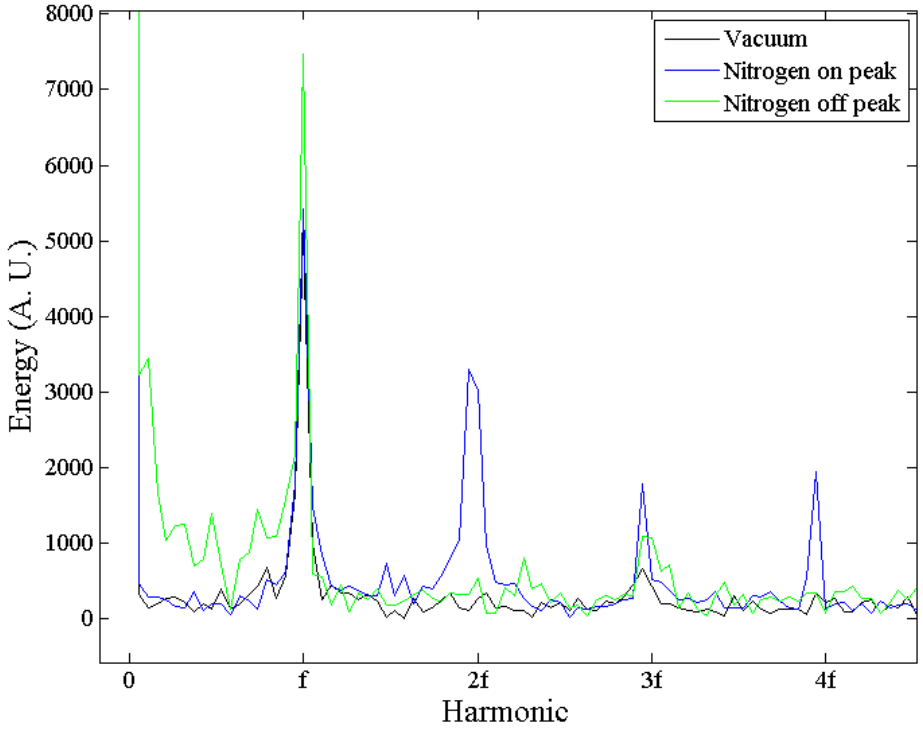

Figure 34 - Second harmonic generation using two filter composite passband

The techniques presented for monitoring a sample gas' concentration are not without their limitations. As demonstrated with the second harmonic generation technique, the wide band fluorescence contributes significant noise when the filter rotation spans more than a nanometer of the spectrum. This effect results from the change in the integrated fluorescence noise captured at the two extreme ends of the rotation. A wider passband will increase the

significance of this effect. The narrow composite passband using two filters has noise problems as a result of the non-linear shift in the center wavelength as described earlier in the section. Although the narrow passband limits the integrated fluorescence, the increased bandwidth change, as shown in Figure 26, counteracts the gains of a narrow passband as the rotational amplitude is increased.

An additional limitation is imposed by the collecting detector. The integration time of the detector must be balanced against the rotation rate of the filters. Enough light must be collected to resolve the concentration with the desired precision while also rotating fast enough to lock into the sinusoidal signal at either f or $2f$ depending on the detection scheme. This aspect of the technique was not examined in these experiments and would likely require further engineering to determine if a suitable balance can be found that yields useful results. The rotational speeds often had periods on the order of 10 seconds which is clearly too slow to meet the requirements specified for the fuel gas detection system.

Finally, the technique is limited to monitoring a single Raman line at a time. Although this may be suitable for many other applications, it is not applicable to sensing fuel gas concentrations without duplicating the platform and isolating individual Raman lines for simultaneous analysis. This could be accomplished using additional filtering or branching with holographic beam splitters, but doing so would minimize or eliminate the cost reduction intended in using the rotating filter platform.

7.0 PRINCIPAL COMPONENT ANALYSIS FOR GAS COMPOSITION

The end use of the Raman sensing system is to accurately characterize the incoming fuel supply for a gas turbine. Capturing the Raman signal as spectroscopic data is only the beginning of the control problem. The actual information of interest to turbine operators is the characteristic flame speed of the fuel. This is often given as the Wobbe index which is derived from the energy content and density of the gas. Determining the Wobbe index from a spectrum requires an accurate method of calculating gas composition. A heuristic approach using the ratio of the spectral peaks and the known gas cross-sections is one viable option and was originally selected due to the simplicity of the method. A more rigorous approach was desired in the hope of improving reliability and accuracy. In this effort, principal component analysis (PCA) was investigated for the ability to accurately map gas composition using a set of pure calibration gases.

Principal component analysis is a multi-variable analysis technique aimed at reducing unwieldy data sets to a manageable number of variables. In the case presented here, the more than one thousand data points from the CCD array, as formed by the summation of the rows, are reduced to a set of variables equal to the number of gases, usually less than twenty, describing the gas concentrations. The process to accomplish the reduction involves finding the relation between the data sets by taking the covariance, finding the eigenvectors of the covariance matrix, and selecting only the most significant eigenvectors as determined by the magnitudes of the

eigenvalues. In this way, only the significant eigenvectors are needed to represent the initial data set with minimal information loss. These few eigenvectors form a lower dimensional space in which the data is mapped to characterize a sample [14].

The application of PCA in quantifying gases began with investigating how to first identify the gases by spectra alone. This quickly led to algorithms developed for facial recognition as in [15]. There the interest is matching face images with ones stored for comparison. The principle applies in the same way to gas identification so it served as a reasonable starting point for developing a greater understanding of the technique and challenges faced in extending the method to quantify the results. PCA is applied to a set of training data that will form the numerical basis for comparing known and unknown samples. Spectra of pure gases of interest serve as the training data and are simultaneously mapped in the lower dimensional space for comparison with unknown samples.

Preparations for the analysis involve arranging a set of data that will be used to obtain the principal components and serve as calibration data. The data of interest is spectral measurements collected by a CCD array. The 1044 pixels of the array serve as a 1044 dimensional data set describing the composition of the gas. These data sets include spectra for six gases of interest: methane, ethane, propane, carbon monoxide, hydrogen, and nitrogen. Multiple spectra of each sample gas, 10 samples of each were used in the development here, are averaged together to produce a reliable training set free of significant anomalies. Each of the data sets is corrected for detector response using a blackbody source to perform a magnitude correction. The data for each gas is arranged as a column and the full set of six gases forms a 1044 x 6 matrix.

For the work reported here, some of the points do not include meaningful data as only a few peaks are important in determining concentrations. These points introduce additional noise

in the compiled data set so the data is trimmed to 940 points to remove the unneeded points which consist mostly of dark and fluorescence noise. Points outside of the Raman peaks of interest are used to produce a 6^{th} order polynomial fit to subtract out the dark and fluorescence noise from the Raman peaks. A similar polynomial fit is applied to remove the silica Raman signature as well. The resulting noise-subtracted Raman peak's magnitude is now a linear representation of the gas concentration. The process is performed for each calibration gas to produce a blackbody corrected, noise subtracted, reduced data matrix which will be called *A* which has a reduced size of 940 x 6 after preparation. The algorithm begins by normalizing the data sets by performing a mean subtraction where the mean is found by averaging the 6 data sets for each spectral point. This eliminates the means' effect on the principal components as it is the relationship between the data that is desired. With the data normalized, it is now possible to take the covariance and find the eigenvectors. For the definition of *A* provided above, the covariance matrix of the data set for performing PCA is expressed as AA^T. The covariance matrix is a square matrix with a size determined by the number of pixels retained from the CCD array spectrum, for example 940 x 940. The actual number of pixels used in the calculations can be on the order of 900 for typical CCD arrays as in the calculations performed on the training set for developing the algorithm. The covariance matrix will therefore have nearly a million entries and require significant processing time to find the eigenvectors.

It is possible to reduce the processing requirements by reconsidering what information we seek as [15] notes that for a small number of data sets with many points direct PCA is extremely inefficient. The direct covariance matrix produces as many eigenvectors as there are points in the data set, most of which have a corresponding eigenvalue equal to zero indicating no significance is contained in the corresponding eigenvector. There are only M-1 meaningful

eigenvectors where M is the number of training data sets [15]. A simplification in the calculations is accomplished by producing a reduced set of M eigenvectors, where M is the 6 training gases used in the analysis, by performing PCA on the transpose of the training data:

$$A^T A v = \lambda v$$

where $A^T A$ is a reduced covariance matrix of size 6 x 6, λ are the eigenvalues, and v are the reduced set of eigenvectors. The 6 most significant principal eigenvectors can be found easily by multiplying both sides by the spectral data:

$$A A^T A v = \lambda A v$$

where Av are now the principal eigenvectors, which will be called u, of AA^T the original covariance matrix of the training data set.

The principal eigenvectors $u = Av$, size 940 x 6, and the calibration set of gases, size 940 x 1 for each gas, together are used to form a 6-dimensional space. The calibration set includes some of the primary gases of interest for the Raman sensor system: methane, ethane, propane, hydrogen, nitrogen, and carbon dioxide. A complete set would also require oxygen for maximum accuracy though a sample was not available at the time of development of the algorithm. The formation of this space is completed by a simple vector multiplication:

$$\Omega_i = \left(u^T(\Gamma - \mu)\right)^T$$

where Γ is the data set for comparison, μ is the mean of the training data formed earlier in first normalizing the data (these are both matrices 940 x 1), and Ω is a row vector representing the projection of the data into the 6-dimensional space. This calculation is repeated for each calibration gas to form the vectors Ω_1 through Ω_6 and any experimental sample to be characterized to form the vector Ω_S.

At this point, gas samples can be identified by calculating the Euclidean distance between the Ω mappings for the sample and each of the calibration gases. This is the interest of [15] for facial recognition; however, the calculations must be taken a step further to quantify the composition of the sample in terms of fractions of the calibration samples. First the vectors corresponding to the calibration gases are formed into a matrix:

$$B = \begin{bmatrix} \Omega_1 \\ \Omega_2 \\ \vdots \\ \Omega_6 \end{bmatrix}$$

Since all spectra are corrected with a blackbody comparison and have the fluorescence noise subtracted by a polynomial fit, the measured Raman peaks correlate linearly with gas concentration. The mapping of the data to the 6-dimensional space is also a linear process so a mixed gas sample of concentrations ρ is expected to map to Ω_S that is a linear combination of the vector mappings in *B*:

$$\Omega_S = [\rho_1 \; \rho_2 \; \cdots \; \rho_6] * B$$

The gas concentrations defined in ρ are then found by determining the coefficients of this linear combination:

$$\rho = \Omega_S * B^{-1}$$

The resulting concentrations are in the form of a fraction of the concentration of the calibration sample. To determine the true percentage composition of the gas, ρ must be normalized to unity by dividing by the sum of the individual concentrations ρ_i.

The complete algorithm was tested at first with 10 spectra, of each constituent, averaged together to form the training data. Then virtual gas samples were formed using these same spectra. Virtual gas samples were formed by taking a spectrum from each of the six gases and adding them together. Thus each virtual gas mix consisted of equal concentrations of the six

gases. The ten sets of gas spectra gave us ten implementations of this virtual, equal concentration mix of the six gases. Table 3 shows the error of the algorithm using each of the 10 sets of gas data individually as test gases to be analyzed. The synthesized gas mixture should ideally produce results with "concentrations" of 1 for each gas with a small error as a result of deviations introduced by the random fluctuations of noise between individual samples and the training set mean. Lacking any optimization, a significant error exists in each of the nitrogen measurements and lesser errors for hydrogen and carbon dioxide. The errors are far larger than the 1 percent precision desired of the system so a method to optimize the process was developed to minimize this error.

Table 3 – Numeric percentage error with direct PCA before optimization

Gas sample set	N_2	CH_4	C_2H_4	C_3H_6	H_2	CO_2
Set 1	25.7	0.3	0.7	-0.2	2.7	5.5
Set 2	-82.4	-0.8	-0.1	0.0	-5.7	-17.6
Set 3	32.1	0.4	0.1	-0.2	1.4	7.7
Set 4	16.3	0.2	0.0	0.0	1.2	4.7
Set 5	26.7	0.3	0.1	0.2	1.1	5.8
Set 6	35.0	0.8	0.9	-0.2	2.2	8.2
Set 7	16.9	0.1	0.2	0.0	1.0	4.1
Set 8	33.2	0.1	0.7	0.0	2.2	5.9
Set 9	-53.7	-0.4	-1.4	0.0	-2.8	-13.4
Set 10	-49.8	-0.8	-1.3	0.4	-3.3	-10.9

Minimizing the error began with the prediction that the source of the deviation is a combination of the effects of imperfect numeric precision and the large differences in the scales of the individual input data sets, for example the nitrogen spectral peak is roughly a factor of seven smaller than that of methane. Working under this assumption, the input data used to train

the algorithm was scaled by constants in order to adjust the relative significance of each principal eigenvector. An initial test of multiplying the nitrogen scale showed improvement in accuracy so a more rigorous test was prepared. The basic algorithm was repeated with a series of multiplying constants to minimize the error in the ten data sets tested in the algorithm. The minimization was performed by summing the variances of the results for each gas. The constant that produced the smallest sum of the variances was stored. The process was repeated to find the best fit constant for each of the six training gases. That training set was used to "analyze" each of the ten virtual gas mixtures. These results are shown in Table 4. Only four cases have "concentration" errors larger than one percent.

Table 4 - Optimized algorithm output error

Gas sample set	N_2	CH_4	C_2H_4	C_3H_6	H_2	CO_2
Set 1	-0.40	-0.09	0.47	-0.19	1.04	-0.52
Set 2	-0.86	0.31	0.70	-0.05	-0.28	0.93
Set 3	-0.17	0.04	-0.23	-0.15	-0.51	0.97
Set 4	0.83	0.00	-0.17	0.08	0.14	1.05
Set 5	0.52	0.20	-0.21	0.39	-0.19	-0.32
Set 6	-0.98	-0.04	0.62	-0.36	-0.72	-0.26
Set 7	-0.80	-0.23	0.07	-0.06	-0.45	-0.50
Set 8	0.38	-0.36	0.29	0.07	0.04	-2.00
Set 9	0.87	0.18	-0.76	-0.14	0.70	-0.37
Set 10	0.60	-0.01	-0.78	0.42	0.24	1.02

The primary measure of the accuracy of this technique is how well it handles random samples. For simplicity, the data tested in all cases above were taken from the same set as used to form the training set. From a calibration perspective, it makes sense to use the same data to determine the multiplying constants that minimize the error. To verify the accuracy of the process for gas samples outside of the calibration set, a separate set of data not used in the

training set was analyzed using the algorithm. This test would reveal how well the system characterizes random samples of mixed gases during operation. Table 5 shows the results of three such samples analyzed with the optimized algorithm. The results show that even though the error is insignificant in most cases in the training set, the error within the samples remains significant (>4%).

Table 5 - Sample gas output error

Gas sample set	N_2	CH_4	C_2H_4	C_3H_6	H_2	CO_2
Sample 1	-4.23	-0.73	0.23	-0.29	-2.24	-1.58
Sample 2	-3.91	-0.52	0.03	-0.50	-1.02	-0.72
Sample 3	-0.67	-0.41	-0.37	0.16	-1.29	-1.24

Whether these errors are acceptable for turbine control is reliant on the impact on the Wobbe index. Table 5 does show that the hydrocarbons have small enough errors to have little impact on the Wobbe index. The errors in the minority gases have a lesser effect and they account for a smaller fraction of the typical fuel gas composition. A more thorough accuracy analysis of the current numerical method of extracting concentrations using peak magnitudes is required to perform a complete comparison of each algorithm's strengths and weaknesses.

8.0 SUMMARY AND FUTURE WORK

This body of work has presented numerous techniques that expand the use of Raman spectroscopy to real-time analyses for gaseous systems. The noise analysis of the hollow waveguide-based Raman sensor has introduced the use of the silver colloidal paint at the pump input end of the capillary to reduce optically excited noise. Low cost waveguide fabrication was explored to cut system costs, gain a greater understanding of the quality of the surface finish required for effective waveguides, and reduce the dependence on the limited suppliers of high quality hollow waveguides. Characterization and verification of the Raman collection efficiency in capillary waveguides enabled the accurate simulation of potential replacement guides with unique dimensions and surface materials. These simulations aid in system design and optimization when working with unfamiliar configurations. A novel technique was presented for measuring Raman signals in the presence of significant optically excited noise by modulating the pass band of an optical filter to reject this noise. Finally, an algorithm using principal component analysis was developed that accurately measures the composition of a sample gas by extracting the unique features that define the individual component gases in the recorded spectrum.

Research and development of the colloidal paint and waveguide mode analysis are complete; though the other projects have additional work to consider in the future. The waveguide fabrication by pumping abrasives through the silver capillaries was moderately successful. The technique produced waveguides of a high enough quality to transmit 85% of the

input pump light. Although the results were not useful for our application due to the low transmission at high angles to the guide's axis, the technique could prove useful for waveguide fabrication for other applications. Additional work is required to achieve high quality waveguides suitable for the Raman sensor. A direction for new work was discussed in Section 4 where it was suggested that a replacement pump capable of higher flow rates be used in the polishing system. Such an investigation would confirm if the use of a turbulent flow of the abrasive would reduce the losses for higher order propagating modes sufficiently for use in Raman collection.

The use of tunable filters as a spectrometer-free substitute in a form of wavelength modulation spectroscopy is a new idea that requires additional study to maximize its usefulness. The use of a rotary stage enabled tuning of the filters accurately but not quickly. Alternative hardware or novel configurations are needed to speed up the acquisition of data so that the sinusoidal signal is detectable using a lock-in amplifier rather than relying on the signal processing used in this work. One possible enhancement to speed up the response would be to use an acousto-optic filter as it can be tuned electrically at a higher frequency than the rotational stage with angle-tuned filters. The technique does not eliminate detector noise so optimization of the sensor requires a balance between integration time and rotation rate based on the speed and accuracy the selected detector.

The application of principal component analysis to determine gas composition from a recorded spectrum comes with the numerical inaccuracies associated with multivariable analysis using noisy data. A method of reducing the variations in measurements was demonstrated, although a more thorough analysis of the mathematics may reveal further means of reducing the error. The accuracy obtained may be sufficient for many applications in which case the limited

processing required may provide quicker results than other algorithms. Extending the work in fuel gas analysis will require a look at the effect of the error on the predicted Wobbe index. Such effect is the main interest of turbine operators and the result is not immediately clear without further analysis of the results and implementation of the algorithm in a test system.

The developments presented here have found a place as part of research shared with the National Energy Technology Lab. Some of the work has already been incorporated in a test bed for the technology which will enter live system testing on a running turbine. The combined efforts contribute to a system that may see commercial viability within a few years.

BIBLIOGRAPHY

[1] E. B. Overton, K. R. Carney, N. Roques, and H. P. Dharmasena, "Fast GC instrumentation and analysis for field applications," *Field Analytical Chemistry & Technology*, vol. 5, no. 1-2, pp. 97-105, May 2001.

[2] L. E. Sieker, "Composition Analysis in Pipeline Gas & NGL with Process Mass Spectrometry," AMETEK, White paper 2006.

[3] Thomas Engel, *Quantum Chemistry and Spectroscopy*.: Prentice Hall, 2005.

[4] (2009, September) Wikipedia. [Online]. http://en.wikipedia.org/wiki/File:Raman_energy_levels.svg

[5] M. P. Buric, K. P. Chen, J. Falk, and S. D. Woodruff, "Enhanced spontaneous Raman scattering and gas composition analysis using a photonic crystal fiber," *Applied Optics*, vol. 47, no. 23, pp. 4255-4261, August 2008.

[6] W. R. Fenner, H. A. Hyatt, J. M. Kellam, and S. P. S. Porto, "Raman cross section of some simple gases," *Journal of the Optical Society of America*, vol. 63, no. 1, pp. 73-77, January 1973.

[7] Polymicro Technologies. (2011, July) Polymicro Technologies Products. [Online]. http://www.polymicro.com/products/products.htm

[8] C. E. Morrow, O. Gregory, P. Bhardwag, G. Gu, and M. B. Bauman, "Monolithic Hollow Waveguide And Method And Apparatus For Making The Same," Patents: Optical Waveguides 5,325,458, June 28, 1994.

[9] Y. A. Cengel and J. M. Cimbala, *Fluid Mechanics Fundamentals and Applications*.: McGraw-Hill, 2006.

[10] M. P. Buric, K. P. Chen, J. Falk, and S. D. Woodruff, "Multimode metal-lined capillaries for Raman collection and sensing," *Jounal of the Optical Society of America B*, vol. 27, no. 12, pp. 2612-2619, November 2010.

[11] E. A. J. Marcatili and R. A. Schmeltzer, "Hollow Metalic Waveguides for Long Distance Optical Transmission and Lasers," *The Bell System Technical Journal*, pp. 1783-1809, July 1964.

[12] Semrock. (2011, July) Semrock. [Online]. http://www.semrock.com/FilterDetails.aspx?id=TBP01-620/14-25x36

[13] J. A. Silver, "Frequency-modulation spectroscopy for trace species detection: theory and comparison among experimental methods," *Applied Optics*, vol. 31, no. 6, pp. 707-717, February 1992.

[14] L. I. Smith. (2002, February) Department of Computer Science - Otage University. [Online]. http://www.cs.otago.ac.nz/cosc453/student_tutorials/principal_components.pdf

[15] A. Pentland M. Turk, "Eigenfaces for Recognition," *Journal of Cognitive Neuroscience*, vol. 3, no. 1, pp. 71-86, 1991.